

# The $\rho$ Oph region revisited with Gaia EDR3

## Two young populations, new members, and old impostors

Natalie Grasser<sup>1</sup>, Sebastian Ratzenböck<sup>2</sup>, João Alves<sup>1,2,3</sup>, Josefa Großschedl<sup>1</sup>, Stefan Meingast<sup>1</sup>, Catherine Zucker<sup>4</sup>, Alvaro Hacar<sup>1</sup>, Charles Lada<sup>4</sup>, Alyssa Goodman<sup>3,4</sup>, Marco Lombardi<sup>5</sup>, John C. Forbes<sup>6</sup>, Immanuel M. Bomze<sup>2</sup>, and Torsten Möller<sup>2</sup>

<sup>1</sup> University of Vienna, Department of Astrophysics, Türkenschanzstrasse 17, 1180 Wien, Austria  
e-mail: natalie.grasser@univie.ac.at

<sup>2</sup> Data Science at University of Vienna, Währinger Straße 29, 1090 Vienna, Austria

<sup>3</sup> Radcliffe Institute for Advanced Study, Harvard University, 10 Garden Street, Cambridge, MA 02138, USA

<sup>4</sup> Center for Astrophysics | Harvard & Smithsonian, 60 Garden St., Cambridge, MA 02138, USA

<sup>5</sup> University of Milano, via Celoria, 16, I-20133 Milano, Italy

<sup>6</sup> Flatiron Institute, Simons Foundation, 162 Fifth Avenue, New York, NY 10010, USA

### ABSTRACT

**Context.** Young and embedded stellar populations are important probes of the star formation process. Their properties and the environments they create have the potential to affect the formation of new planets. Paradoxically, we have a better census of nearby embedded young populations than the slightly more evolved optically visible young populations. The high accuracy measurements and all-sky coverage of *Gaia* data are about to change this situation.

**Aims.** This work aims to construct the most complete sample to date of YSOs in the  $\rho$  Oph region.

**Methods.** We compile a catalog of 761 Ophiuchus YSOs from the literature and crossmatch it with the *Gaia* EDR3, *Gaia*-ESO and APOGEE-2 surveys. We apply a multivariate classification algorithm to this catalog to identify new, co-moving population candidates.

**Results.** We find 173 new YSO candidates in the *Gaia* EDR3 catalog belonging to the  $\rho$  Oph region. The new sources appear to be mainly Class III M-stars and substellar objects and are less extincted than the known members. We find 19 previously unknown sources with disks. The analysis of the proper motion distribution of the entire sample reveals a well-defined bimodality, implying two distinct populations sharing a similar 3D volume. The first population comprises young stars' clusters around the  $\rho$  Ophiuchi star and the main Ophiuchus clouds (L1688, L1689, L1709). In contrast, the second population is older ( $\sim 10$  Myr), dispersed, has a distinct proper motion, and is likely part of the Upper-Sco group. The two populations are moving away from each other at about 3.8 km/s, and will no longer overlap in about 4 Myr. Finally, we flag 47 sources in the literature as impostors, which are sources that exhibit large deviations from the average distance and proper motion properties of the  $\rho$  Oph population. Our results show the importance of accurate 3D space and motion information for improved stellar population analysis.

**Key words.** astrometry – methods: data analysis – stars: formation – stars: pre-main sequence

## 1. Introduction

Since the development of millimeter-wave receivers and infrared detectors in the 1970s, local star formation studies have mostly concentrated on the densest star-forming structures in molecular clouds. Successive generations of instruments have opened a fundamental window into molecular cloud structure, cloud fragmentation and collapse, and have unveiled the dust enshrouded young stellar object (YSO) populations in nearby clouds. This approach has generated an almost paradoxical situation where we currently know more about the very young dust-obscured populations than we know about the more evolved and optically revealed population in nearby star-forming regions.

More evolved YSOs show less infrared-excess emission and escape detection in IR surveys but are critical to reconstructing a region's star formation history. Therefore, identifying the young optically visible population is essential for reconstructing a star formation event. Moreover, sources in the unobscured environments of nearby star-forming gas include some of the lowest-mass objects (brown dwarfs and planetary-mass objects) and some of the closest proto-planetary disks we can study, the lat-

ter becoming important targets for resolved ALMA studies (e.g., [ALMA Partnership et al. 2015](#)) in the sub-millimeter wavelength range.

Optical data from the *Gaia* mission ([Gaia Collaboration et al. 2016](#)), with its exquisite sensitivity and all-sky coverage, have changed this situation. The mission has brought a breakthrough in studying the gas shape and motion ([Großschedl et al. 2018, 2020](#)) and young stellar structures not previously known ([Meingast et al. 2019, 2020](#)) since its second data release *Gaia* DR2. In this work, we revisit one of the nearest star-forming regions, the  $\rho$  Ophiuchi region, by using the newly available *Gaia* EDR3 data ([Gaia Collaboration et al. 2020](#)).

The  $\rho$  Ophiuchi ( $\rho$  Oph) star forming region ([Wilkings et al. 2008](#)) is one of the nearest active star-forming regions at a distance of approximately 139 pc ([Lombardi et al. 2008; Zucker et al. 2020](#)). It comprises the cluster of young stars around the  $\rho$  Ophiuchi star ([Pillitteri et al. 2016](#)) and the young stars associated with the dense gas in the Ophiuchus cloud complex, mainly the L1688, L1689 and L1709 clouds ([Loren 1989a,b](#)). Due to its youth and proximity to Earth, it has played an essential role

in many star formation studies, in particular in the definition of the YSO classes (Wilking & Lada 1983; Lada & Wilking 1984; Andre et al. 1993; Greene et al. 1994).  $\rho$  Oph is located in the foreground of the south-eastern edge of Upper Scorpius, which is a subgroup of the Scorpius-Centaurus OB association, and has a distance of around 145 pc (Wilkinson et al. 2018). It has long been suspected that star formation in the  $\rho$  Oph region has been triggered by feedback from massive stars from Upper Sco (Vrba 1977; Loren & Wootten 1986; Loren 1989a,b; de Geus 1992).

The youngest stars in the region are associated with the densest gas in the Ophiuchus cloud complex, mostly L1688, with an average age of about 0.3 Myr (Greene & Meyer 1995; Luhman & Rieke 1999), while the stellar population on the lower column density surface has an average estimated age of 2 to 5 Myr (Wilking et al. 2008; Erickson et al. 2011). There are three main dark clouds in the  $\rho$  Oph complex, namely the Lynds dark clouds L1688, L1689 and L1709 (Lynds 1962; Loren 1989a,b). The large column-density towards particular regions in these clouds, where the optical extinction can reach values up to  $A_V$  above 40 – 50 mag (Wilking & Lada 1983; Wilking et al. 1989; Lombardi et al. 2008), make infrared (IR) observations essential for studying the embedded young stellar population in the cloud. There is a rich embedded cluster of YSOs in L1688, which is mostly invisible at optical wavelengths and whose stars have not dispersed yet (Ducourant et al. 2017).

In this paper we apply the recently developed method from Ratzenböck et al. (2020) to *Gaia* EDR3 data, to unveil the most complete sample to date of YSOs towards the  $\rho$  Oph region. The method uses the astrometric properties of known YSOs in combination with a bagging classifier of one-class support vector machines (OCSVM) on *Gaia* EDR3 data to perform a 5D search (3D positions and 2D proper motions) for possible new population members. The algorithm creates a hyper surface around the positional and proper motion distribution of the input samples in a 5D space to find new sources with similar properties. Radial velocities of the input population are also necessary for constraining the models.

In Sect. 2 we present the data used in this work, which includes known sources from the literature, which we cross-matched with further astronomical surveys. In Sect. 3 we summarize how the classification algorithm operates to identify new sources. We present the results of the algorithm in Sect. 4, including a detailed analysis. In Sect. 5 we discuss some implications of our findings.

## 2. Data

### 2.1. Literature catalog

In this section we summarize how we compiled our literature catalog of  $\rho$  Oph sources. This work is based on studies of  $\rho$  Oph and L1688 from 11 papers, which are summarized in Table 1, including the number of sources utilized from each work. We assign each paper a number for citation purposes in our final catalog. Some papers also include sources from IR observations, which are essential for a complete sample due to the high optical extinction in the region. The highest number of sources are provided by Esplin & Luhman (2020), Cánovas et al. (2019), and Wilking et al. (2008). Duplicates were removed with an internal match within a 1.0 arcsec match radius and an internal match on the *Gaia* source IDs. Our result is a final literature table of 761 unique sources.

Additionally, three surveys were selected for cross-matching with our literature sample to obtain astrometric data (proper mo-

tions, parallaxes, and radial velocities) of the sources, which is essential for identifying new sources with the algorithm. The *Gaia* (Gaia Collaboration et al. 2016) survey provides us with unprecedented astrometry with improved quality and statistics compared to any previous comparable survey, such as *Hipparcos* (Perryman et al. 1997). Therefore, proper motions and parallaxes were obtained from *Gaia* EDR3 (Gaia Collaboration et al. 2020). To complement *Gaia* astrometry and constrain the models of the algorithm, we combine it with radial velocities from APOGEE-2 (Majewski et al. 2017), a large-scale spectroscopic survey conducted in the near-infrared, and *Gaia*-ESO (Gilmore et al. 2012), a spectroscopic survey by the European Southern Observatory (ESO) combined with the *Gaia* astrometry catalog. Radial velocities from these surveys deliver superior resolution and statistics compared to radial velocities from *Gaia*.

A cross-match of the literature sources with data from *Gaia* EDR3 yielded a total of 368 matches, which is 48.4 % of the entire literature sample, leaving many sources without *Gaia* equivalents. One explanation for this is that *Gaia* is only sensitive to optical wavelengths, while many of the obtained literature sources are too embedded in the cloud and can only be observed at IR wavelengths. Additionally, several sources, such as from Esplin & Luhman (2020), are brown dwarfs, which are often too faint to be seen by *Gaia*. A cross-match with APOGEE-2 resulted in 132 matches, while a cross-match with *Gaia*-ESO data yielded 60 matches in our literature catalog. For sources with multiple measurements, higher priority was given to surveys with higher accuracy. Therefore we use *Gaia* proper motions and parallaxes over those obtained from the literature. For sources with multiple radial velocity values, data from *Gaia*-ESO has the highest priority, followed by APOGEE and *Gaia*.

The distances to the sources were calculated through the inverse of the parallax, which is a good approximation for the distance to the region (130–140 pc) (e.g., Luri et al. 2018). Furthermore, the tangential velocities  $v_\alpha$  and  $v_\delta$ , as well as their errors, were calculated through the proper motions and parallaxes, as shown in Equations A.1–A.4. For a better overview, we list the symbols and abbreviations of frequent parameters used throughout this paper:

- $\alpha, \delta$  (deg): right ascension and declination
- $l, b$  (deg): galactic longitude and latitude
- $\varpi$  (mas): parallax of the sources
- $d$  (pc): distance to the sources, inverse of parallax
- $\mu_\alpha^*$  (mas/yr):  $\mu_\alpha \cos(\delta)$ , proper motion along  $\alpha$
- $\mu_\delta$  (mas/yr): proper motion along  $\delta$
- $v_r$  (km/s): heliocentric radial velocity
- $v_\alpha, v_\delta$  (km/s): tangential velocities along  $\alpha$  and  $\delta$
- $v_l, v_b$  (km/s): tangential velocities along  $l$  and  $b$
- $X, Y, Z$  (pc): positions in Galactic Cartesian coordinates, where  $X, Y$ , and  $Z$  point towards the Galactic center, the direction of the Galactic rotation, and the North Galactic Pole, respectively
- $U, V, W$  (km/s): velocities in Galactic Cartesian coordinates

### 2.2. Impostors and suspicious sources

We have discovered several sources within the literature catalog that have properties that do not fit very well to the region’s average astrometric values. In the Appendix A, we list the interval ranges in which most of the distance, radial velocity, and tangential velocity values in  $\rho$  Oph are found. All of the sources which have at least one of these values outside our defined intervals we identify as potential misclassifications and label them

**Table 1:** Overview of the literature used to collect sources of the  $\rho$  Ophiuchi region, including the methods that were used and the amount of sources we obtained from each paper.

Paper	Method	Sources used	Ref
<a href="#">Greene et al. (1994)</a>	mid-IR photometric study	60	1
<a href="#">Haisch et al. (2002)</a>	near- and mid-IR observations	14	2
<a href="#">Padgett et al. (2008)</a>	Multiband Imaging Photometer for <i>Spitzer</i> (MIPS)	132	3
<a href="#">Wilking et al. (2008)</a>	X-ray and IR photometric and spectroscopic surveys	316	4
<a href="#">Evans et al. (2009)</a>	<i>Spitzer</i> c2d Legacy survey	292	5
<a href="#">Dunham et al. (2015)</a>	<i>Spitzer</i> c2d and GB Legacy surveys	292	6
<a href="#">Rigliaco et al. (2016)</a>	dynamical analysis with <i>Gaia</i> -ESO survey	45	7
<a href="#">Ducourant et al. (2017)</a>	near-IR observations to determine proper motions	93	8
<a href="#">Cánovas et al. (2019)</a>	density-based clustering algorithms with <i>Gaia</i> DR2	467	9
<a href="#">Sullivan et al. (2019)</a>	radial velocity survey with data from IR spectrographs	35	10
<a href="#">Esplin &amp; Luhman (2020)</a>	astrometry from <i>Gaia</i> DR2, proper motions from <i>Spitzer</i>	373	11

as impostors in our catalog. We find 47 of such impostor candidates among the literature sources. Since our intervals are more or less arbitrarily defined, we choose not to remove these impostors from our catalog. Instead, we create a separate column named “Impostors”, in which impostor sources are labeled with a “1”, while all others are labeled with a “0”.

We also looked into sources in the literature without proper motion measurements, mostly extincted sources not in *Gaia*. These are much harder to evaluate since they are mostly faint and have infrared photometry only. Still, some of these are suspicious members. For example, there is a row of six sources towards the tail of the B45 filament from the [Padgett et al. \(2008\)](#) *Spitzer* survey that are seen against relatively low values of dust extinction. Of these six sources, one is a carbon star at 1.3 kpc (THA 23-18), labeled as an impostor because of its distance, while the other five have no detection in any other catalog in CDS, except for a (faint) IRAS detection. Given that these sources are not deeply embedded in a molecular cloud core or clump, it is fair to flag them as suspicious YSOs. They could still be very low mass brown dwarfs, or free floating planetary mass objects, but they suspiciously look like background galaxies. For sources like these we create a separate column named “Suspicious” and labeled the suspicious sources with a “1”.

### 3. Methods

In our work, we applied the classification strategy described in [Ratzenböck et al. \(2020\)](#) for identifying new members of the  $\rho$  Oph region in the *Gaia* EDR3 catalog. The goal of [Ratzenböck et al. \(2020\)](#) was to model the extent of the Meingast 1 stellar stream ([Meingast et al. 2019](#)) in the combined space of proper motions and positions and subsequently use it to infer new members in *Gaia* DR2. The model consists of multiple one-class support vector machine (OCSVM) classifiers in a bagging ensemble.

#### 3.1. Training set selection

To provide reliable sources for the classification algorithm, we created a training set by removing outliers and applying quality cuts. The quality cuts are described in Appendix A, where we also present the training set. To guarantee a high-fidelity training set, we limit our selection to sources with radial velocity measurements. Since the hypersurface created by the OCSVM algorithm depends heavily on the distribution of peripheral sources, it is susceptible to outliers. The use of a soft-margin SVM somewhat mitigates this, but to further reduce the effect of potential

contaminants on the final model shape, we removed the most extreme outliers from the training set as well. To do so, we estimate the local outlier factor ([Breunig et al. 2000](#)) of each source in 5D and remove 5 % of the training set with the highest outlier factor. This removal leads to a final training set of 94 sources, which corresponds to 12.4 % of the literature sample.

#### 3.2. Model selection and prior assumptions

Due to the high model flexibility of OCSVMs, choosing adequate model parameters is critical to guarantee a suitable description of the stellar system. Instead of directly selecting models in the OCSVM hyperparameter space, [Ratzenböck et al. \(2020\)](#) have suggested to constrain models via prior assumptions they have to adhere to, implicitly tuning the model parameters. In addition, as summary statistics, prior assumptions are usually much easier to interpret compared to the original OCSVM parameters. Each set of prior beliefs corresponds to a distribution of allowed models in the input parameter space, such that there is a mapping from a prior assumption tuple to regions in the OCSVM parameter space which contain models that adhere to the given rule set. Instead of explicitly characterizing this map, we sample uniformly from the OCSVM hyperparameter space and remove unfit models. In order to determine a set of prior assumptions for identifying new, high fidelity  $\rho$  Oph members, we consider their application in [Ratzenböck et al. \(2020\)](#). The prior assumptions were motivated by the training set selection process. Since only sources with radial velocities were previously identified to be part of the Meingast 1 stream, the authors formulated prior assumptions based on completeness arguments regarding radial velocities. Specifically, the goal was to find still unknown members without radial velocity measurements, which were confined to the training set extent. However, the  $\rho$  Oph training set selection function is much more complex as we combine radial velocity information across multiple data surveys. This also means we have much less information about potentially concealed  $\rho$  Oph members. Therefore, we adjust the previous assumptions to the  $\rho$  Oph population. In the following, we briefly discuss the selection of the prior assumptions.

##### 3.2.1. Population size

Firstly, we aim to restrict the number of sources a model infers. Because the  $\rho$  Oph population has been studied extensively - with some studies using *Gaia* data as well - we do not expect to find a dramatic increase in overall population size. Based on the number of *Gaia* sources in the training sample, 368, we estimate



a very conservative upper limit of a maximum population size of about twice the sources to be predicted by a single model, setting it to 800 maximal members.

We note here that the prior assumption restrictions only applies to single models, meaning the model ensemble, as a final classifier, can exceed individual or multiple prior assumption limits.

### 3.2.2. Contamination fraction

Secondly, we constrain the contamination fraction of predicted sources across models. The contamination fraction is determined via the 3D velocity distribution of  $\rho$  Oph candidate sources. Precisely, we first model the 3D velocity distribution of the training samples as a single Gaussian distribution. The mean and covariance matrix are determined by maximizing the likelihood of the training data. Subsequently, we define the contamination as the fraction of sources outside the  $3\sigma$  (99.7 %) range of the training set. In practice, we observe very few radial velocities in the predicted set for a single model, and, therefore, the contamination fraction assumption has a minor effect for removing single models. This effect is highlighted in Figure C.1, where we see an almost constant and maximal number of models adhering to the contamination rule for various maximal values. Since the influence is small across such a large range we set it to a value of 15 %.

### 3.2.3. Estimated extent

Lastly, we want to constrain the extent of inferred  $\rho$  Oph members in position and proper motion space. This is done by measuring the dispersion and systematic shift between training and inferred member distributions. We characterize the dispersion in position and proper motion space by the mean deviation of its member stars to their centroid. The prior assumption corresponds to a constraint on the ratio between the average predicted deviation by the average training deviation. For further details, we refer to Appendix B in Ratzenböck et al. (2020). In the case of  $\rho$  Oph, we cannot give a concrete estimate on the expected extent of unknown members in position and proper motion space. Instead, we motivate a range of maximal values. We postulate a constraint on the parameter to be within 1, which constrains the predicted extent to the training set extent, and 2 where models can have twice the dispersion of the training set. We explicitly separate the positional from the proper motion axes since both dispersion measures have physically different meanings, and we might want to restrict one more than the other.

To avoid systematic shifts of the predicted to the training set distribution, we constrain the distance between the centroids of the training and inferred sources. We measure the centroid distance in terms of the mean deviation of the training set sources. A value of one would correspond to a centroid shift with a distance of one mean deviation from the training centroid. Again, finding a precise value is not straightforward, as the value cannot be properly inferred for the unknown  $\rho$  Oph population. Therefore, we limit the maximum shift parameter to a range between 0.1 and 0.7, which we consider already a quite large systematic deviation from the training set.

### 3.3. Building the $\rho$ Oph classifier

We subsequently search for model ensembles within these three parameters, the mean deviation in position, proper motions, and

the maximal systematic shift, while keeping the other two prior assumptions, the maximum number of inferred sources, and the maximum contamination fraction, fixed. As stated in Sect. 3.2.1, a prior assumption tuple corresponds to a model ensemble that adheres to the respective beliefs. For each of these ensembles, we determine a stability threshold by minimizing the Kullback–Leibler (KL) divergence (Kullback & Leibler 1951) between the 3D velocity distributions of training and predicted  $\rho$  Oph members (see Appendix E for more details). We randomly select 100 prior assumption tuples within their respective range, resulting in 100 model ensembles with a corresponding stability threshold.

To select single or multiple suitable classifiers from this space of model ensembles, we consider the following. We aim to maximize the number of inferred  $\rho$  Oph sources while minimizing the number of contaminants in our final prediction set. Thus, we study the distribution of the number of inferred sources over the contamination fraction across the 100 model ensembles. The contamination fraction is determined via the ratio of inferred sources outside the  $3\sigma$  range of the training velocity distribution. The distribution of the 100 randomly sampled model ensembles can be seen in Figure D.1. We observe a clear trend for low-contamination models, which tend to have tighter positional and velocity constraints. Interestingly, these models show a clear mode of the mean systematic shift limit which appear at around 0.28. This sample of low-contamination models are identifying possibly new  $\rho$  Oph members in a non-symmetric region around the training set. To construct the final classifier, we combine the predictions of the 27 models with the lowest contamination fraction of approximately 16.5 %, corresponding to the left-most column of models in the top row of Figure D.1. Finally, we determine a stability threshold for the final ensemble following the procedure outlined in Appendix E. Doing so, we obtain a stability threshold of 13 %. To properly validate the final classifier, we have to consider previously untouched information, the distribution of sources in the Hertzsprung–Russell Diagram (HRD). In order for inferred sources to be actual members of the Rho Oph population, they must follow the same isochrone as the training set. Therefore, we determine the residuals of inferred sources to the best fitting isochrone on the training set, where we obtained an age of about 5 Myrs, and compare them to the training set residuals. In Figure F.1, the standard deviation of training set residuals and inferred residuals can be seen, highlighting an almost perfect agreement with the training data across the full stability range.

## 4. Results

In this section we present the results of the algorithm. Sources from the literature are labeled as “Known” while the new sources are labeled as “New”. The following plots in this section show the known sources in blue, the new sources in red, and a control sample in gray, labeled as “Control”, which serves as a comparison. The control sample was selected in a relatively dust-free region to the West of  $\rho$  Oph at the same galactic latitude. Its galactic coordinates lie between  $346^\circ \leq l \leq 349^\circ$  and  $15^\circ \leq b \leq 18^\circ$ .

### 4.1. Predicted sources

A total of 554 sources in the *Gaia* EDR3 catalog were predicted by the algorithm as belonging to the  $\rho$  Oph region, based on the properties of the training set. The predicted sources include a total of 250 new sources that are not in any of the  $\rho$  Oph catalogs from the literature. A total of 304 of the predicted sources

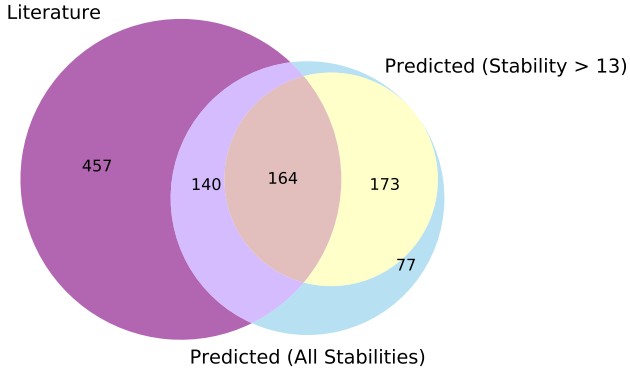


**Fig. 1:** Venn diagram depicting the amount of sources in the literature sample, the predicted sample, and the amount of sources both of them have in common.

are already part of the literature sample of 761 known sources, meaning that 39.9 % of the literature sources were recovered by the algorithm.

Only the sources with a stability > 13 %, namely 173 of the new sources, are considered in the following results. These new sources together with the known ones result in 934 total sources in the  $\rho$  Oph region, while when excluding impostors and suspicious sources we end up with 807 high probability members. In our final catalog, we also include the new sources predicted by the algorithm with a stability < 13 %, resulting in a table of 1011 total sources. Figure 1 visualizes the amount of shared sources in the literature and the prediction set in a Venn diagram, showing sources with a prediction stability > 13 % and all stabilities. More information on the stability can be found in Appendix E. An overview of the final numbers of sources per (sub)sample is given in Table 3. A column overview of the final master catalog of the  $\rho$  Oph young stellar members is presented in Appendix I.

A probable reason for the relatively small overlap in Figure 1 (the algorithm only predicts 39.9 % of the known sources from the literature) is the fact that many of the literature sources were obtained through IR surveys, since embedded stars in  $\rho$  Oph cannot be detected at optical wavelengths. Furthermore, some sources from the literature are impostors, as described in Sect. 2.2. It is also important to note that only 368 literature sources (48.4 %) have *Gaia* EDR3 IDs. Therefore, the algorithm has effectively recovered 82.6 % of literature sources that are in *Gaia* EDR3. 25 of these 68 literature sources that are in *Gaia* EDR3 but were not predicted by the algorithm do not have *Gaia* parallaxes. *Gaia* is an optical telescope, hence it is insensitive to high extinction sources in the L1688 dense clump, where the peak of the surface density of YSOs in the cloud complex is located (e.g., Ortiz-León et al. 2017; Ducourant et al. 2017). Sources not visible at optical wavelengths cannot be predicted by the algorithm.

#### 4.2. Astrometric properties

Figure 2 shows the distribution of the  $\rho$  Oph sources in galactic coordinates with the known sources in blue and the new ones in red. The 94 sources in the training set, labeled as “Train”, are included as unfilled black squares for comparison. As can be seen in the figure, the new sources are more dispersed, with many of them being shifted towards the North, West, and South

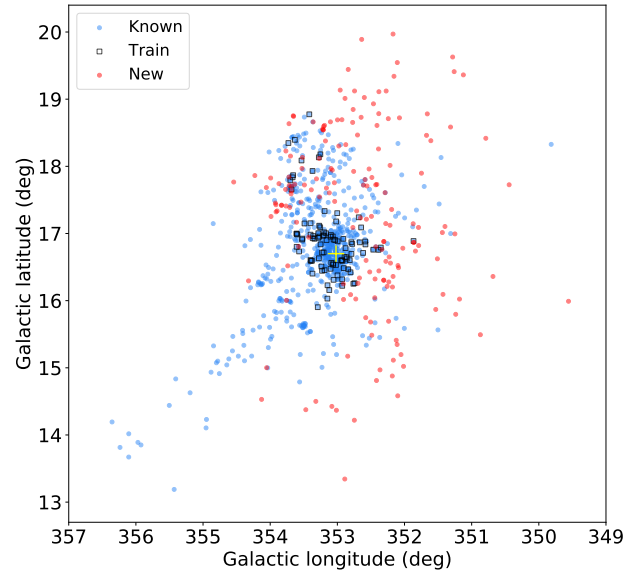


**Fig. 2:** Distribution of  $\rho$  Oph sources in galactic coordinates. The known sources from the literature are in blue, while new sources are in red. Sources from the training set are represented by black squares. The approximate location of the extinction peak is marked by a yellow cross.

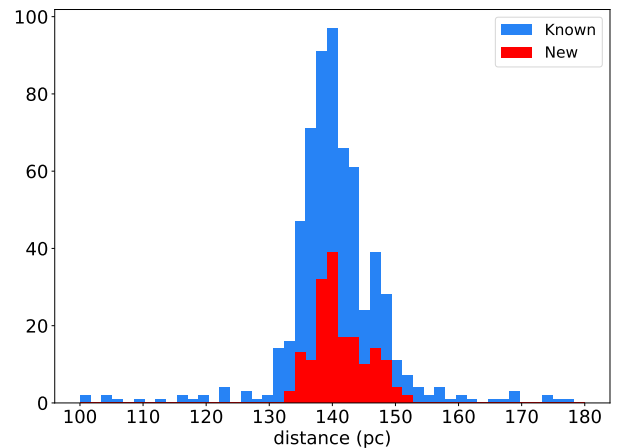


**Fig. 3:** Histogram of distances to the  $\rho$  Oph sources. The distribution of the known sources from the literature is in blue, while the new sources are in red.

of the known sources. Hardly any new sources were found near the core of the cloud and towards the East. The extinction peak of the L1688 cloud, marked by a yellow cross in the figure, lies at around  $l \approx 353.0^\circ$  and  $b \approx 16.7^\circ$  (Alves et al., in prep). It is most likely responsible for the lack of new sources in the core, since sources with a high optical extinction cannot be detected by *Gaia*.

Figure 3 shows a histogram of the distances to the  $\rho$  Oph sources, which were determined through the inverse of their parallaxes. Most of the sources are clustered around a mean distance of approximately 140 pc (see Table G.1), which agrees well with the literature value of around 139 pc (Zucker et al. 2020). No further correlations were found between the sources constituting the small peak at around 147–148 pc. In general, the average astro-

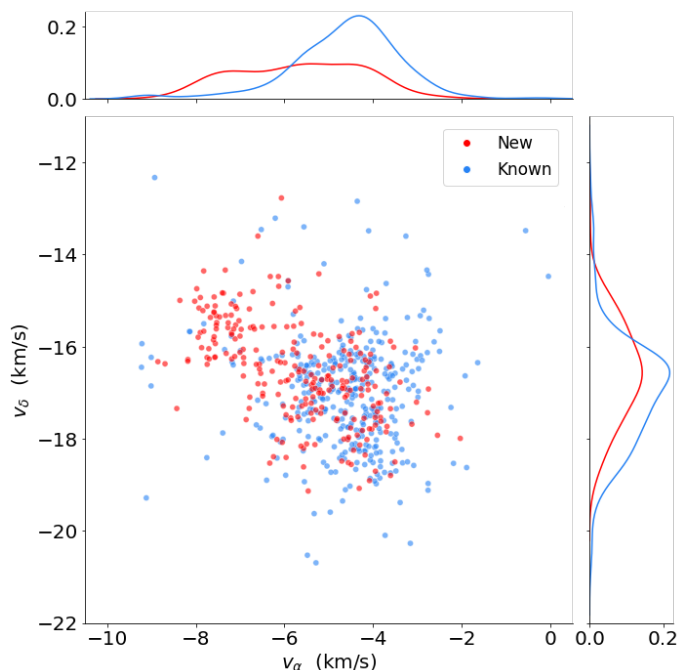


**Fig. 4:** Tangential velocities of the  $\rho$  Oph sources, including their marginal distributions. The known sources are shown in blue, while the new sources are shown in red.

metric properties of the known and new sources are very similar and overlap within  $\pm 1\sigma$  (see Table G.1), further confirming that they belong to the same region.

Figure 4 shows the tangential velocity distribution of the  $\rho$  Oph sources, including their marginal distributions. The impostor sources (see Sect. 2.2) from the literature are not included in the diagram, to avoid the influence of outliers. Although the distribution of the new sources shows a significant overlap with that of the known sources, a large part of the population is slightly shifted towards more negative values of  $v_\alpha$  and more positive  $v_\delta$ , hinting at more than a single population. As can be seen in the marginal distributions of the new sources, their curves are flatter and encompass different values due to this second dynamical population.

For further analysis of this distinct kinematic subgroup, we determined the angles between the proper motion vectors ( $\mu_{\alpha*,\delta}$ ) and the  $\alpha$ -axis ( $\theta_{\alpha,\text{obs}}$ ), and added these values to our table in a new column for all the sources with proper motion measurements. Analyzing these angles in a histogram reveals the two dynamically different populations as two distinct peaks. To disentangle these two populations, we use the angle distribution as visual aid and apply a cut from  $112^\circ < \theta_{\alpha,\text{obs}} < 121^\circ$ , resulting in a subgroup of 103 sources for the second population. Only sources with *Gaia* proper motions are considered for the second population to keep the selection as conservative as possible, since non-*Gaia* proper motions are substantially noisier. Using the proper motion angles in different parameter spaces produces the same result, as shown in the histograms in the bottom row of Fig. 5. The distribution of angles between the proper motion vectors and the  $l$ -axis, for observed velocities and velocities relative to the local standard of rest ( $\theta_{l,\text{obs}}$  and  $\theta_{l,\text{LSR}}$ ), reveal the same kinematic substructure as the two distinct peaks in Fig. 4.

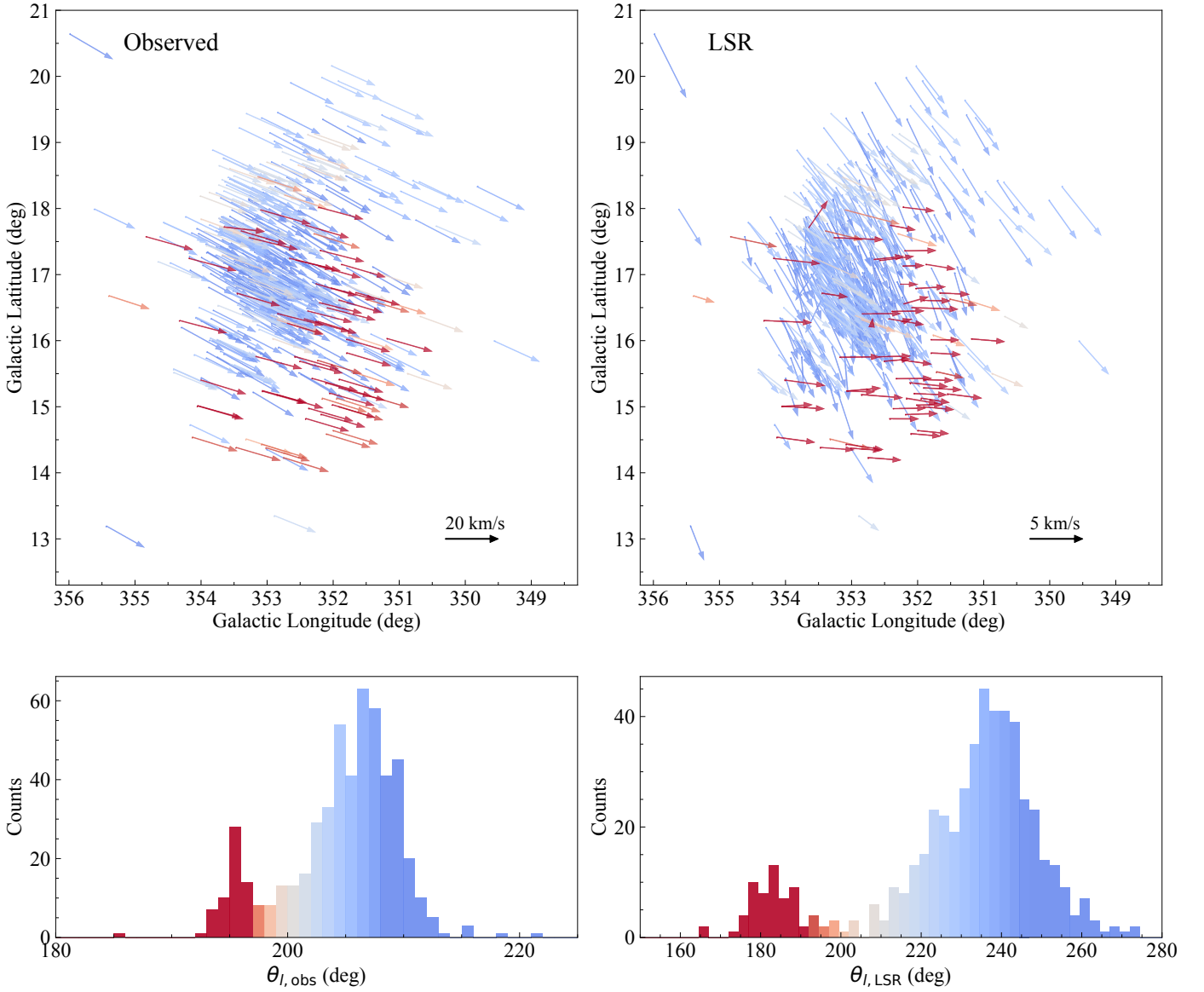
Fig. 5 highlights the influence of the Sun’s reflex motion on the observed proper motions. The top panels show the direction of motion using the observed velocities (left) and the direction

of motion when correcting for the Sun’s motion (right), with the latter showing a clearer separation between the two populations. Still, to separate the two populations we used the observed proper motion to avoid injecting in the final selection uncertainties related to the Sun’s motion (Schönrich et al. 2010). Nevertheless, making the selection of the populations in  $\theta_{l,\text{LSR}}$  would not change significantly the result.

For further discussion, this second dynamically distinct population shall be referred to as “Pop 2”, while the remaining shall be referred as “Pop 1” sources, after excluding impostors and suspicious sources (see Sect. 2.2). By construction, Pop 2 only contains sources with proper motions from *Gaia*, since those are more accurate, in order to include only high-fidelity sources in the newly discovered population. We like to point out that there are 18 literature sources with proper motions that would be classified as Pop 2 according to their angles ( $112 < \theta_{\alpha,\text{obs}} < 121$ ). These 18 sources have proper motion measurements from Ducourant et al. (2017) and are located in the core of the L1688 cloud, meaning that these embedded YSOs (not visible in the optical) rather belong to the slightly younger Pop 1 (see Fig. H.1). Therefore, we do not include these 18 sources in Pop 2 since the accuracy of the ground-based proper motion measurements are not comparable to *Gaia* EDR3 proper motions, and they remain a part of Pop 1 in our classification. Concluding, we define the sources in Pop 1 to be all sources from our  $\rho$  Oph catalog excluding impostors, suspicious sources, and Pop 2 sources. This population comprises the clusters of young stars around the  $\rho$  Ophiuchi star and the main Ophiuchus clouds (L1688, L1689, L1709). Finally, we identify 100 sources in Pop 2 and 784 in Pop 1 when including sources of all stabilities. When applying a cut at stability  $> 13\%$  we are left with 70 sources in Pop 2 and 737 sources in Pop 1 (see Table 3).

The 100 sources in Pop 2 coincide with the sources whose tangential velocities create the second dynamical structure in Figure 4. In other words, the two sub-populations seen in this Figure and the bimodal angle distribution consist of the same stars. 79 of these 100 sources (79 %) are new sources identified by the algorithm. Further examination of this subgroup reveals that unlike Pop 1, Pop 2 sources are mostly dispersed and are distributed relatively evenly all around the core of the cloud (see Fig. 10), apart from a tentative clustering towards the Galactic south-west. Their distances exhibit a similar distribution to the other  $\rho$  Oph sources, which shows that the two populations occupy approximately the same 3D volume.

Table 2 shows the average values of the distances, proper motions, radial velocities, Galactic Cartesian positions  $X, Y, Z$  and Galactic Cartesian velocities  $U, V, W$ , as well as their standard deviations of the two populations (Pop 1 and Pop 2) in the  $\rho$  Oph region. To avoid the influence of outliers, impostors are not included in the computation of these average values. The average 3D positions of the two populations only exhibit small deviations, showing that they are not merely a 2D overlap, but mixed in all three spatial dimensions. As can be seen from the proper motions and tangential velocities in the table, the Pop 2 sources exhibit slightly different dynamical properties, which set them apart. Although the  $U$  and  $V$  velocities of the two populations hardly differ from each other, they also occupy different regions in the  $UVW$  velocity space because of the larger differences in  $W$ . However, the bimodality seen in Fig. 4 is not so evident in the  $UWV$  space, possibly because only 11 sources (11 %) from the second population have  $UVW$  velocities. By computing the difference between the  $UVW$  vectors of the two populations, we find that they are moving away from each other at about 3.8 km/s and will no longer overlap in about 4 Myr.



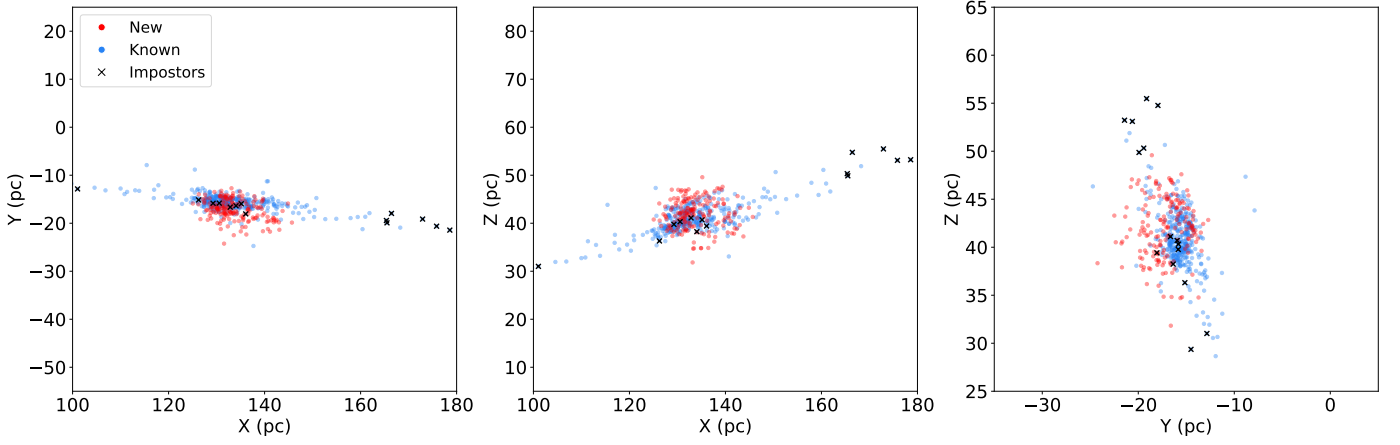
**Fig. 5:** Analysis of the two populations in  $\rho$  Oph based on their proper motion. *Top row:* Galactic distribution of the known and new  $\rho$  Oph members, including all new sources (without stability cut), while suspicious sources and impostors are excluded. Arrows represent the tangential velocity vectors, color-coded for the angle between the vectors and the  $l$ -axis ( $\theta_{l,\text{obs}}$  and  $\theta_{l,\text{LSR}}$  in left and right panel, respectively). The left panel shows the observed tangential velocity vectors ( $\mathbf{v}_{\text{obs}}$ ), as derived from *Gaia* EDR3 parameters ( $v_l$ ,  $v_b$ ), the right panel shows the tangential velocity vectors relative to the local standard of rest ( $\mathbf{v}_{\text{LSR}}$  based on  $v_{l,\text{LSR}}$ ,  $v_{b,\text{LSR}}$ ). The black arrows in the bottom right corners indicate the vector length for velocities of 20 km/s and 5 km/s for  $\mathbf{v}_{\text{obs}}$  and  $\mathbf{v}_{\text{LSR}}$ , respectively. These reference vectors have an angle of  $180^\circ$  relative to the  $l$ -axis. *Bottom row:* Histograms showing the distributions of angles  $\theta_{l,\text{obs}}$  and  $\theta_{l,\text{LSR}}$  for the sources as in the top panels. The bin size in the left histogram have a width of  $1^\circ$  and in the right histogram of  $2.5^\circ$ , since  $\theta_{l,\text{LSR}}$  covers a larger range of angles. The histograms are color-coded for the angles as in the top panels.

Figure 6 shows the Galactic Cartesian coordinates of the known and new  $\rho$  Oph sources for a visualization of their 3D distribution. The literature sources exhibit a more elongated distribution, even beyond the limits of the figure. Some of the deviating sources are labeled as impostors in Sect. 2.2 and are marked with black crosses in Fig. 6. The elongation is most prominent along the line of sight, which is mostly caused by the larger errors in the parallax measurements compared to celestial coordinates, while some of the elongation is caused by outliers.

#### 4.3. Observational HRD

Figure 7 shows an observational Hertzsprung-Russell Diagram (HRD) of the  $\rho$  Oph sources with the known sources in blue and the new ones in red. To create the diagram, we use the *Gaia* passbands  $G$  versus  $G - G_{RP}$ . Using the observed magnitudes  $m_G$  in the  $G$  band and the individual distances  $d$  of the sources, we computed the absolute magnitudes  $M_G$  in the  $G$  band with  $M_G = m_G + 5 - 5 \log_{10} d$ . The photometric values are obtained from *Gaia* EDR3 for both the  $\rho$  Oph and the control sample. Since *Gaia* EDR3 photometry is affected by systematic errors, corrections were applied to the  $G$  band as described in [Riello](#)





**Fig. 6:** Galactic Cartesian coordinates of the  $\rho$  Oph sources. The known sources from the literature are in blue, while the new sources are in red, and impostor sources (see Section 2.2) are marked with black crosses (see legend). Several sources from the literature fall outside the figure, and are also labeled as impostors.

**Table 2:** Average positional and dynamical properties including their standard deviations ( $1\sigma$ ) for the two populations (Pop 1 and Pop 2) in the  $\rho$  Oph region.

Dimension	Pop 1	Pop 2
$\alpha$ (deg)	$246.0 \pm 0.4$	$246.7 \pm 1.1$
$\delta$ (deg)	$-23.8 \pm 0.7$	$-24.9 \pm 1.1$
$\varpi$ (mas)	$7.2 \pm 0.3$	$7.0 \pm 0.4$
$d$ (pc)	$139.5 \pm 6.4$	$143.0 \pm 7.2$
$\mu_\alpha^*$ (mas/yr)	$-7.0 \pm 1.5$	$-10.9 \pm 1.2$
$\mu_\delta$ (mas/yr)	$-25.7 \pm 1.3$	$-22.9 \pm 1.7$
$v_\alpha$ (km/s)	$-4.6 \pm 1.0$	$-7.4 \pm 0.8$
$v_\delta$ (km/s)	$-17.0 \pm 1.1$	$-15.5 \pm 1.1$
$v_r$ (km/s)	$-4.6 \pm 3.2$	$-3.5 \pm 4.0$
$X$ (pc)	$131.9 \pm 6.0$	$136.0 \pm 7.0$
$Y$ (pc)	$-15.6 \pm 1.6$	$-17.5 \pm 2.3$
$Z$ (pc)	$42.5 \pm 2.4$	$40.6 \pm 3.4$
$U$ (km/s)	$-4.6 \pm 2.8$	$-4.1 \pm 3.7$
$V$ (km/s)	$-15.2 \pm 1.0$	$-15.9 \pm 1.3$
$W$ (km/s)	$-9.1 \pm 1.1$	$-5.4 \pm 1.0$

et al. (2020). Furthermore, quality cuts like in Großschedl et al. (2020), which are listed in Appendix B, were applied to *Gaia* photometry of the  $\rho$  Oph and control sample to include only high quality measurements.

To estimate an average age for the stellar population we used isochrones from the PARSEC models (Marigo et al. 2017) for *Gaia* EDR3 photometry. An extinction vector in the  $V$  passband, labeled as  $A_V$ , is shown to visualize the direction and magnitude of extinction in this color-magnitude space using the reddening law for the  $G$  and  $RP$  passbands from Cardelli et al. (1989) and O'Donnell (1994) provided by PARSEC. Two equal-mass-curves for sources with  $0.09 M_\odot$  (solar masses) and  $1 M_\odot$  are shown in orange.

As seen in the observational HRD, some of the new sources appear to be slightly older than the known sources, while the two samples largely overlap. Their distribution is consistent with earlier work of Luhman & Rieke (1999) and Esplin & Luhman (2020), who find ages of 0.3–6 Myr for  $\rho$  Oph sources. Most of the new sources are low mass stars, probably consisting mainly of M-type spectral classes or substellar objects.

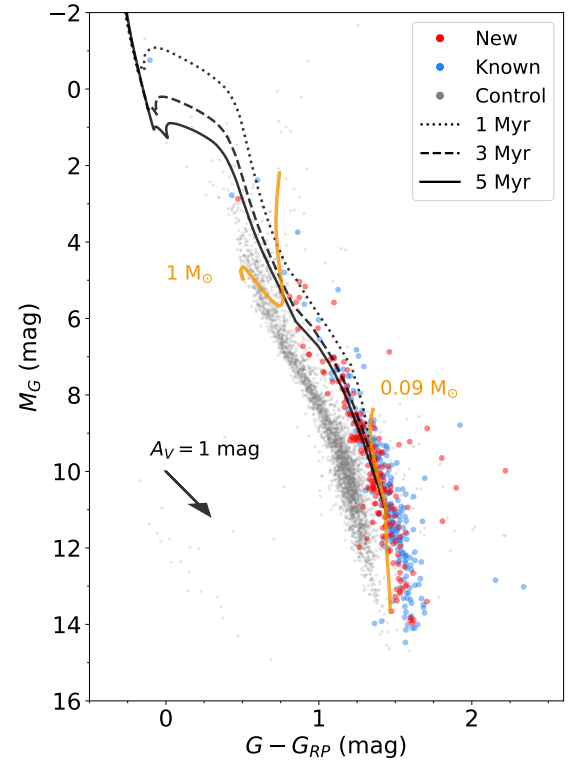


**Fig. 7:** Observational HRD for known (blue) and new (red) sources of  $\rho$  Oph, and the control sample (gray), with corrections applied to the  $G$  passband. An extinction vector with  $A_V = 1$  mag is shown as a black arrow. The isochrones correspond to ages of 1, 3 and 5 Myr, while the iso-mass lines of  $0.09 M_\odot$  and  $1 M_\odot$  include stars with ages from 0.1 to 100 Myr.

For completeness, an observational HRD of the two dynamical populations in the  $\rho$  Oph region is shown in Fig. H.1. We use  $G_{BP} - G_{RP}$  instead of  $G - G_{RP}$  for this HRD because it shows a clearer separation of the two populations. The second population appears to be older and align better with the 10 Myr isochrone. To determine an approximate age of the second pop-



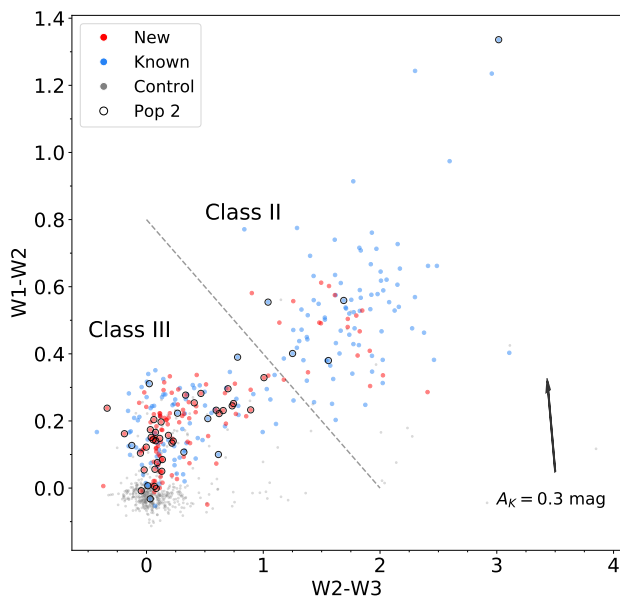


**Fig. 8:** Color-color diagram of the known  $\rho$  Oph sources in blue and the new ones in red, including the control sample in gray, using the W1, W2, and W3 passbands from WISE. The sources comprising the second population (Pop 2) are marked by black circles. An extinction vector in the  $K_S$  passband, labeled as  $A_K$ , is also included. The sources above the dashed line are YSOs with disks, while those below are Class III YSOs.

ulation, we compute a least mean square fit to the data using the  $G$ ,  $BP$  and  $RP$  passbands from *Gaia* to isochrones with solar metallicity from the PARSEC models (Bressan et al. 2012). Using only high-fidelity sources with the quality cuts of stability  $> 13$ , ruwe  $< 1.4$  and astrometric\_sigma5d\_max  $< 0.5$  (for definitions of used *Gaia* parameters, see Table I.1), we obtain an approximate age of 10 Myr for the second population.

#### 4.4. Analysis of infrared colors: infrared excess sources

Using infrared measurements, the presence of protoplanetary disks and envelopes around young stars, including their evolutionary stages, can be inferred. Disks and envelopes emit light in IR wavelengths due to their warm dust emission. A cross-match with data from WISE (Wright et al. 2010), in our case the *All-WISE* catalog, provides stars with the required infrared photometry to analyze IR excesses. This cross-match was carried out using the gaiadr2.allwise\_best\_neighbour IDs provided in the *Gaia* archive. The W1, W2, and W3 passbands correspond to wavelengths of  $3.4 \mu\text{m}$ ,  $4.6 \mu\text{m}$ , and  $12 \mu\text{m}$ , respectively. In order to use only high quality measurements in our diagram, we only included sources above a specific signal-to-noise ratio (SNR). Sources had to fulfill  $w1snr > 10$ ,  $w2snr > 10$ , and  $w3snr > 7$  for the W1, W2, and W3 passbands. This cut was applied to the  $\rho$  Oph and the control sample.

Figure 8 shows a color-color diagram for  $W1 - W2$  versus  $W2 - W3$ , with the known sources in blue and the new ones in red. The control sample is included in gray, and the sources of the second population (Pop 2) are marked by black circles. The extinction vector in the  $K$  passband, labeled as  $A_K$ , was determined using the reddening law for the W1, W2, and W3 passbands as

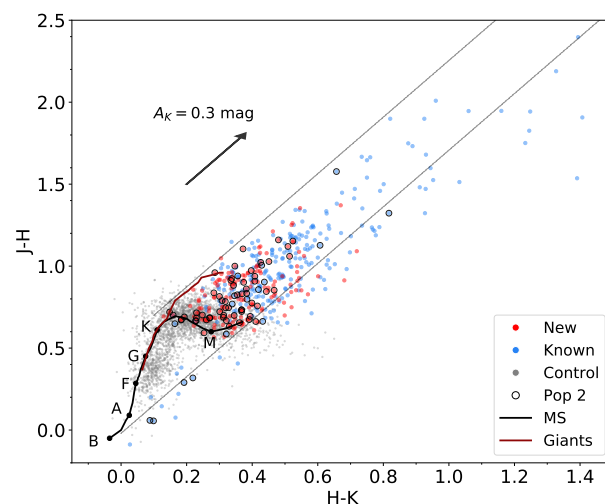


**Fig. 9:** Color-color diagram of the  $\rho$  Oph sources in blue and red, including the control sample in gray and the sources from the second population (Pop 2) as black circles, using the  $J$ ,  $H$  and  $K_S$  passbands from 2MASS. The main sequence (MS) and the giant branch from Bessell & Brett (1988) are included in the diagram, as well as an extinction vector in the  $K_S$  passband, labeled as  $A_K$ . The two parallel lines with the slope of the extinction enclose reddened main sequence stars.

in Meingast et al. (2018). A dashed line, serving as a rough estimate, separates two regions in the diagram, namely those with and without IR excess, as similarly done in Koenig & Leisawitz (2014). Sources further to the top and right in the diagram exhibit an IR excess and are therefore most likely YSOs with disks (Class II), which exhibit a circumstellar disk, similar to Classical T Tauri stars (Greene et al. 1994).

As seen in the diagram, the Pop 2 sources exhibit less IR-excess compared to Pop 1, confirming that Pop 2 includes overall more evolved stellar members and is therefore likely older. Additionally, we have found 19 new sources with potential disks, which corresponds to a disk fraction of about 11 % in the new sources, considering that we have 173 new sources in total. Further analysis of these 19 Class II YSOs reveals that they are located further away from the core of the cloud, which might explain why they have not been found in any previous IR studies of  $\rho$  Oph. Most of the new sources have little or no IR excess, which could be the likely reason why they have not been identified in any previous infrared surveys. Sources below the dashed line are either Class III YSOs or main sequence stars. As Figure 7 confirms that  $\rho$  Oph consists mainly of young stars, this implies that the  $\rho$  Oph sources below the line can only be Class III YSOs, which are associated with tenuous disks or bare photospheres, therefore creating no detectable infrared excess (Cánovas et al. 2019). We conclude that we have found 69 new Class III YSOs in Ophiuchus. The fraction of Class II to Class III YSOs is around 0.28 in the new sources, 0.89 in the known sources, and around 0.63 in the entire population. An overview of the final numbers is given in Table 3.

Cross-matching our sample with data from 2MASS (Skrutskie et al. 2006) using the gaiadr2.tmass\_best\_neighbour IDs in the *Gaia* archive provides us with further IR measurements in the  $J$ ,  $H$ , and  $K_S$  passbands, which correspond to wave-

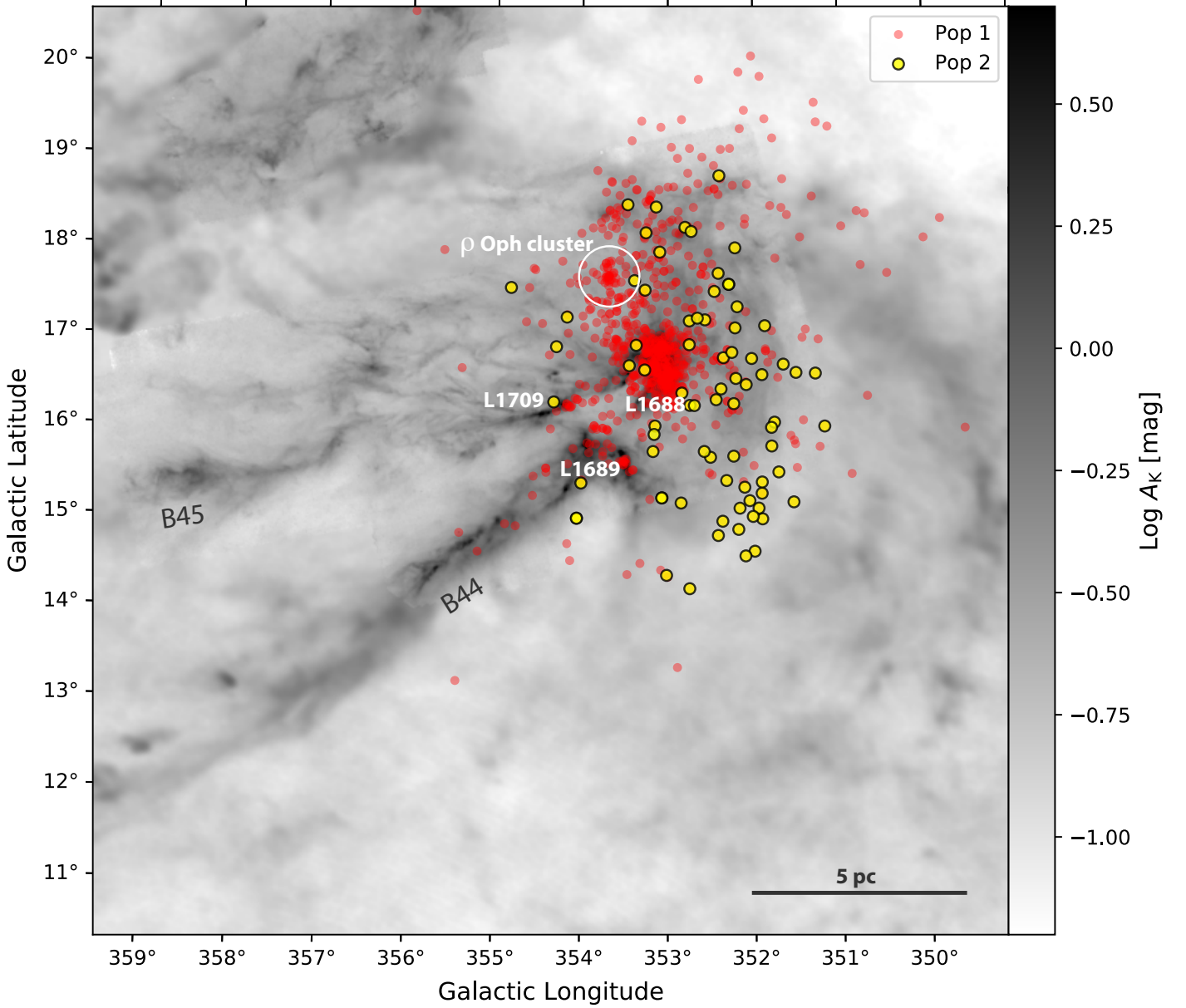


**Fig. 10:** Spatial distribution of the two dynamical populations in  $\rho$  Oph in red and yellow circles. The  $\rho$  Oph cluster, centered on the  $\rho$  Ophiuchi star, is marked by a white open circle. The actively forming clouds, L1688, L1689, and L1709, are also marked. Impostors and suspicious sources (see Sect. 2.2) are not included in this figure. The background grayscale is a column density map of Ophiuchus made with Herschel, Planck, and 2MASS data (Alves et al., in prep).

lengths of  $1.25\ \mu\text{m}$ ,  $1.65\ \mu\text{m}$ , and  $2.17\ \mu\text{m}$ , respectively. Figure 9 shows a color-color diagram of  $H - K_S$  versus  $J - H$ . The known, new, and control sources are in blue, red, and gray, respectively, while the sources from the second population (Pop 2) are marked by black circles. The main sequence (MS) and giant branches are included in the diagram, as determined by Bessell & Brett (1988). The extinction vector in the  $K_S$  passband, labeled as  $A_K$ , was determined using the reddening law for the  $J$ ,  $H$  and  $K_S$  passbands by Meingast et al. (2018). Two parallel lines with the slope of the extinction vector were added to enclose reddened sources above the main sequence. As can be seen from their position in the diagram, most of the known and new sources are M-stars. Furthermore, the new sources are, on average, less extinguished than the known ones, as would be expected, since they were selected based on the *Gaia* catalog.

## 5. Discussion

In this work, we applied the classification strategy developed by Ratzenböck et al. (2020) to identify new members of the  $\rho$  Oph region in *Gaia* EDR3. This method yielded 173 new members with similar properties in position and tangential velocity to the known sources from the literature. From these results, we were able to create a master catalog of all known sources in  $\rho$  Oph, including our new sources from *Gaia* EDR3. This so far most complete sample of  $\rho$  Oph contains 934 sources in total (1011 including the new sources with a stability  $< 13$ ).

### 5.1. The $\rho$ Oph region is a mixture of two young populations

The tangential velocity distribution of the final sample, presented in Fig. 4, reveals structure hinting at the presence of more than

**Table 3:** Final numbers of sources resulting from our  $\rho$  Oph stellar member analysis.

(Sub)sample	N
Known literature selected sources	761
Literature selected sources with measured Gaia EDR3 parallax	368
Literature selected sources without impostors or suspicious sources	634
Impostor sources in the literature	47
Suspicious sources in the literature	80
All new sources without stability cut	250
New sources with stability cut	173
New sources with circumstellar disks (Class II)	19
Total number of $\rho$ Oph sources without stability cut	1011
Total number of $\rho$ Oph sources with stability cut for new sources	934
Total number of $\rho$ Oph sources without impostors and suspicious sources	884
Total number of $\rho$ Oph sources with stability cut and without impostors and suspicious	807
Pop 1 sources without stability cut	784
Pop 2 sources without stability cut	100
Pop 1 sources with stability cut	737
Pop 2 sources with stability cut	70

one population. The bimodal distribution of the proper motion angles presented in Fig. 5 further asserts the existence of two main populations in the surveyed area, which we call Pop 1 and Pop 2. What is discussed in the literature as “ $\rho$  Oph star forming region” or “ $\rho$  Oph core” is in fact a mixture of two populations, with similar but distinct dynamical properties and ages, occupying approximately the same 3D volume. The first (Pop 1), with ages 0.3–6 Myr (Luhman & Rieke 1999; Erickson et al. 2011; Esplin & Luhman 2020), as confirmed in Fig. 7, comprises clusters of young stars around the  $\rho$  Ophiuchi star and the main Ophiuchus clouds, namely L1688, L1689, L1709 (see Fig. 10). The second population (Pop 2) appears dispersed in comparison and has a relatively older age up to about 10 Myr. Given that the age, relative disk fraction, and 2D motion is similar to those of Upper Sco ( $\sim 10$  Myr, Pecaute & Mamajek 2016; Luhman & Esplin 2020), it is possible that the 100 Pop 2 sources in the dispersed population originate from the much larger Upper Sco population toward the Galactic north. This hypothesis will be further examined in future work (Ratzenböck et al. in prep.).

The clear kinematic difference between these two populations, only detectable because of the unprecedented accuracy of *Gaia* EDR3, is the main finding of our study, as it sheds light on the genesis of the  $\rho$  Oph star-forming region. The proper motion distribution found in Fig. 5 translates into a 3D space motion difference between the two populations of about 3.8 km/s. This relative space motion indicates that the regions are moving away from each other and could imply that the origin of the  $\rho$  Oph star-forming region is connected to that of the Upper Sco population. A study of the space motion of the two populations is called for as it will give insights on the origin of the different motions.

The closest ongoing star formation region, the  $\rho$  Oph region, remains a natural laboratory for star formation studies, from core formation and collapse to disk formation and evolution into planets. Our work demonstrates how the unprecedented astrometric precision of *Gaia* is revealing the fine dynamical structure of the nearest star forming regions.

### 5.2. Multiple young populations in star-forming regions

Our finding in this paper of a mixed population in  $\rho$  Oph is similar to the discovery of the foreground population in front of the Orion Nebula (Alves & Bouy 2012; Bouy et al. 2014; Chen et al. 2020). Unfortunately, two of the closest benchmark

star formation regions to Earth, the  $\rho$  Oph region and the Orion Nebula Cluster, are now known to contain multiple young populations, either in projection or intermingled, which complicates the extraction of star formation observables. These two cases are unlikely the exception. Mixed populations are to be expected, for example, in triggered star formation as a previous generation compresses interstellar gas into a new generation of stars. Characterizing the existence of multi-populations in nearby star formation regions is critical because it directly affects the fundamental star formation observables, such as star formation history, rate, efficiency, and the initial mass function (IMF). Looking forward, multiple populations should be looked for in nearby star forming regions, and for at least  $\rho$  Oph and the Orion Nebula Cluster, they need to be disentangled for a precise description of the basic star formation observables.

### 5.3. Caveats

Some of the literature sources are located off from the center of the cloud, in particular the ones that seem to trace the B44 filament (L1689, L1712, L1759), away from the center of the distribution and towards the lower East in Figure 2. These sources might be too far from the cluster center to be considered by the algorithm, since the training set is only located near the center of the distribution (see Figure 2). Still, the sources seen in projection onto B44 are also located at the edge of the proper motion distribution, making them even less likely to be predicted. About half of the literature sources in B44 are either impostors or suspicious sources and are unlikely to be part of  $\rho$  Oph, as discussed in Sect. 2.2. This suggests that the algorithm is not missing a significant number of sources towards the filaments B44 and B45. We checked the sources that project against the B44 filament for possible nebula that could confirm a connection with the cloud, but could not find any. All the six sources associated with the tail of B45 are either impostors (the carbon star THA 23-18, for example) or suspicious.

### 5.4. Comparison with previous work using *Gaia* data

Cánovas et al. (2019) applied several clustering algorithms (DBSCAN, OPTICS, HDBSCAN) and identified 166 new sources in the  $\rho$  Oph region using the *Gaia* DR2 catalog. We have found



sources that were not identified as potential members by Cánovas et al. (2019), despite also running our search algorithm on the *Gaia* DR2 catalog before the availability of *Gaia* EDR3. Our search in only *Gaia* DR2 yielded around 100 new members over the Cánovas et al. (2019) search, depending on how strictly we set our prior assumptions. This substantially larger number of new YSOs from the same data set suggest that our approach is an effective tool for searching for new members of co-moving stellar structures.

Esplin & Luhman (2020) used *Gaia* DR2 data and derived proper-motions with multi-epoch *Spitzer Space Telescope* data to find 155 new young stars, 102 of these associated with the Ophiuchus clouds and 47 with Upper Sco. Unlike our study, Esplin & Luhman (2020) did not use multivariate classification techniques to identify new sources, so we attribute the discovery of the 173 new YSOs over their search to tailored classification techniques as the one described in this paper, which are powerful tools to disentangle stellar populations in the high-precision *Gaia* era data.

Finally, the algorithm from Ratzenböck et al. (2020) has shown to be quite an effective method for identifying stars belonging to a particular population, based on the properties of a sub-sample of known sources. The method was able to identify 173 new optically visible sources in  $\rho$  Oph, providing more information on the optically revealed population of the region. Therefore, we conclude that our method is a useful tool suitable for similar research in the future.

## 6. Conclusions

The main results from this work can be summarized as follows:

1. We searched the literature to construct a catalog of 761 known YSOs towards the  $\rho$  Ophiuchi region. We cross-match this catalog with the *Gaia* EDR3, *Gaia*-ESO, and APOGEE-2 surveys and use it to feed a classification algorithm designed to find new, co-moving, population candidates in *Gaia* EDR3 using a training set of 94 sources.
2. We found 173 new YSO candidates in *Gaia* EDR3 belonging to the  $\rho$  Ophiuchi region. The distribution of the new sources on an HR-diagram is indistinguishable from previously known young stars in the region, validating our selection.
3. The new sources appear to be mainly Class III M-stars and substellar objects and are generally less extincted than the known members. We found 19 new sources with excess infrared emission suggesting the presence of disks.
4. A proper motion analysis of the  $\rho$  Ophiuchi region reveals the presence of two main populations: the first population of 784 sources comprises clusters of young stars around the  $\rho$  Ophiuchi star and the main Ophiuchus clouds (L1688, L1689, L1709), while the second population of 103 sources is older and dispersed, with a similar but distinct proper motion from the first. The second population's age and proper motion are consistent with it being part of the Upper Sco population. Both populations occupy approximately the same 3D volume.
5. The two populations are moving away from each other at about 3.8 km/s, and will no longer be overlapping in about 4 Myr.
6. Future studies of this benchmark region should treat these two populations as separate or risk biasing the star formation observables, such as star formation history, rate, efficiency, and the IMF.
7. The algorithm used in this paper (OCSVM, Ratzenböck et al. 2020) has proven to be an effective method for identifying stars belonging to a particular population, based on the properties of a sub-sample of known sources.

**Acknowledgements.** This project has received funding from the European Research Council (ERC) under the European Union's Horizon 2020 research and innovation programme (grant agreement No. 851435). This research has made use of data from the European Space Agency (ESA) mission *Gaia* (<https://www.cosmos.esa.int/web/gaia>), processed by the Gaia Data Processing and Analysis Consortium (DPAC, <https://www.cosmos.esa.int/web/gaia/dpac/consortium>), as well as data from the European Southern Observatory (ESO) survey *Gaia*-ESO (Gilmore et al. 2012) and the APO Galactic Evolution Experiment APOGEE (Majewski et al. 2017). This research has also made use of data products from the Two Micron All Sky Survey 2MASS (Skrutskie et al. 2006), which is a joint project of the University of Massachusetts and the Infrared Processing and Analysis Center/California Institute of Technology, funded by the National Aeronautics and Space Administration and the National Science Foundation, the Wide-field Infrared Survey Explorer WISE (Wright et al. 2010), which is a joint project of the University of California, Los Angeles, and the Jet Propulsion Laboratory/California Institute of Technology, funded by the National Aeronautics and Space Administration. The astronomical database SIMBAD (Wenger et al. 2000) has also greatly contributed to this work. Furthermore, this research was made possible thanks to the use of TOPCAT (Taylor 2005), an interactive graphical viewer and editor for tabular data, and Python (<https://www.python.org/>), in particular Astropy (Astropy Collaboration et al. 2018), a community-developed core Python package for Astronomy, NumPy (van der Walt et al. 2011), Matplotlib (Hunter 2007) and Seaborn (Waskom et al. 2017), as well as the Aladin Sky Atlas, developed at CDS, Strasbourg Observatory (Bonnarel et al. 2000).

## References

- ALMA Partnership, Fomalont, E. B., Vlahakis, C., et al. 2015, *ApJ*, 808, L1
- Alves, J. & Bouy, H. 2012, *Astron. Astrophys. Suppl. Ser.*, 547, A97
- Andre, P., Ward-Thompson, D., & Barsony, M. 1993, *ApJ*, 406, 122
- Astropy Collaboration, Price-Whelan, A. M., Sipőcz, B. M., et al. 2018, *AJ*, 156, 123
- Bessell, M. S. & Brett, J. M. 1988, *PASP*, 100, 1134
- Bonnarel, F., Fernique, P., Bienaymé, O., et al. 2000, *A&AS*, 143, 33
- Bouy, H., Alves, J., Bertin, E., Sarro, L. M., & Barrado, D. 2014, *Astron. Astrophys. Suppl. Ser.*, 564, A29
- Bressan, A., Marigo, P., Girardi, L., et al. 2012, *MNRAS*, 427, 127
- Breunig, M. M., Kriegel, H.-P., Ng, R. T., & Sander, J. 2000, *SIGMOD Rec.*, 29, 93–104
- Burnham, K. P. & Anderson, D. R. 2002, *Model Selection and Multimodel Inference* (Springer New York)
- Cánovas, H., Cantero, C., Cieza, L., et al. 2019, *A&A*, 626, A80
- Cardelli, J. A., Clayton, G. C., & Mathis, J. S. 1989, *ApJ*, 345, 245
- Chen, B., D'Onghia, E., Alves, J., & Adamo, A. 2020, *Astron. Astrophys. Suppl. Ser.*, 643, A114
- de Geus, E. J. 1992, *A&A*, 262, 258
- Ducourant, C., Teixeira, R., Krone-Martins, A., et al. 2017, *A&A*, 597, A90
- Dunham, M. M., Allen, L. E., Evans, Neal J., et al. 2015, *ApJS*, 220, 11
- Erickson, K. L., Wilking, B. A., Meyer, M. R., Robinson, J. G., & Stephenson, L. N. 2011, *AJ*, 142, 140
- Esplin, T. L. & Luhman, K. L. 2020, *AJ*, 159, 282
- Evans, N. J., Dunham, M. M., Jorgensen, J. K., et al. 2009, *VizieR Online Data Catalog*, J/ApJS/181/321
- Gaia Collaboration, Brown, A. G. A., Vallenari, A., et al. 2020, *arXiv e-prints*, arXiv:2012.01533
- Gaia Collaboration, Prusti, T., de Bruijne, J. H. J., et al. 2016, *A&A*, 595, A1
- Gilmore, G., Randich, S., Asplund, M., et al. 2012, *The Messenger*, 147, 25
- Greene, T. P. & Meyer, M. R. 1995, *ApJ*, 450, 233
- Greene, T. P., Wilking, B. A., Andre, P., Young, E. T., & Lada, C. J. 1994, *ApJ*, 434, 614
- Großschedl, J. E., Alves, J., & Meingast, S. 2020, *arXiv e-prints*, arXiv:2007.07254
- Großschedl, J. E., Alves, J., Meingast, S., et al. 2018, *A&A*, 619, A106
- Haisch, Karl E., J., Barsony, M., Greene, T. P., & Ressler, M. E. 2002, *AJ*, 124, 2841
- Hunter, J. D. 2007, *Computing in Science and Engineering*, 9, 90
- Kamdar, H., Conroy, C., Ting, Y.-S., et al. 2019, *The Astrophysical Journal*, 884, L42
- Koenig, X. P. & Leisawitz, D. T. 2014, *ApJ*, 791, 131
- Kullback, S. & Leibler, R. A. 1951, *Ann. Math. Statist.*, 22, 79



- Lada, C. J. & Wilking, B. A. 1984, *ApJ*, 287, 610
- Lombardi, M., Lada, C. J., & Alves, J. 2008, *A&A*, 480, 785
- Loren, R. B. 1989a, *ApJ*, 338, 902
- Loren, R. B. 1989b, *ApJ*, 338, 925
- Loren, R. B. & Wootten, A. 1986, *ApJ*, 306, 142
- Luhman, K. L. & Esplin, T. L. 2020, *AJ*, 160, 44
- Luhman, K. L. & Rieke, G. H. 1999, *ApJ*, 525, 440
- Luri, X., Brown, A. G. A., Sarro, L., et al. 2018, *Astron. Astrophys. Suppl. Ser.*
- Lynds, B. T. 1962, *ApJS*, 7, 1
- Majewski, S. R., Schiavon, R. P., Frinchaboy, P. M., et al. 2017, *AJ*, 154, 94
- Marigo, P., Girardi, L., Bressan, A., et al. 2017, *ApJ*, 835, 77
- Meingast, S., Alves, J., & Fürnkranz, V. 2019, *A&A*, 622, L13
- Meingast, S., Alves, J., & Lombardi, M. 2018, *A&A*, 614, A65
- Meingast, S., Alves, J., & Rottensteiner, A. 2020, *arXiv e-prints*, arXiv:2010.06591
- O'Donnell, J. E. 1994, *ApJ*, 422, 158
- Ortiz-León, G. N., Loinard, L., Kounkel, M. A., et al. 2017, *ApJ*, 834, 141
- Padgett, D. L., Rebull, L. M., Stapelfeldt, K. R., et al. 2008, *ApJ*, 672, 1013
- Pecaut, M. J. & Mamajek, E. E. 2016, *MNRAS*, 461, 794
- Perryman, M. A. C., Lindegren, L., Kovalevsky, J., et al. 1997, *A&A*, 500, 501
- Petersen, K. B. & Pedersen, M. S. 2012, *The Matrix Cookbook*, version 20121115
- Pillitteri, I., Wolk, S. J., Chen, H. H., & Goodman, A. 2016, *A&A*, 592, A88
- Ratzenböck, S., Meingast, S., Alves, J., Möller, T., & Bomze, I. 2020, *A&A*, 639, A64
- Riello, M., De Angeli, F., Evans, D. W., et al. 2020, *arXiv e-prints*, arXiv:2012.01916
- Rigliaco, E., Wilking, B., Meyer, M. R., et al. 2016, *A&A*, 588, A123
- Schönrich, R., Binney, J., & Dehnen, W. 2010, *MNRAS*, 403, 1829
- Skrutskie, M. F., Cutri, R. M., Stiening, R., et al. 2006, *AJ*, 131, 1163
- Sullivan, T., Wilking, B. A., Greene, T. P., et al. 2019, *AJ*, 158, 41
- Taylor, M. B. 2005, in *Astronomical Society of the Pacific Conference Series*, Vol. 347, *Astronomical Data Analysis Software and Systems XIV*, ed. P. Shopbell, M. Britton, & R. Ebert, 29
- van der Walt, S., Colbert, S. C., & Varoquaux, G. 2011, *Computing in Science and Engineering*, 13, 22
- Vrba, F. J. 1977, *AJ*, 82, 198
- Waskom, M., Botvinnik, O., O’Kane, D., et al. 2017, *Mwaskom/Seaborn: V0.8.1* (September 2017)
- Wenger, M., Ochsenbein, F., Egret, D., et al. 2000, *A&AS*, 143, 9
- Wilking, B. A., Gagné, M., & Allen, L. E. 2008, *Star Formation in the  $\rho$  Ophiuchi Molecular Cloud*, ed. B. Reipurth, Vol. 5, 351
- Wilking, B. A. & Lada, C. J. 1983, *ApJ*, 274, 698
- Wilking, B. A., Lada, C. J., & Young, E. T. 1989, *ApJ*, 340, 823
- Wilkinson, S., Merín, B., & Riviere-Marichalar, P. 2018, *Astron. Astrophys. Suppl. Ser.*, 618, A12
- Wright, E. L., Eisenhardt, P. R. M., Mainzer, A. K., et al. 2010, *AJ*, 140, 1868
- Zucker, C., Speagle, J. S., Schlafly, E. F., et al. 2020, *A&A*, 633, A51

## Appendix A: Training set criteria

In this Appendix we describe the quality cuts determined for the training set, which are used in the classification algorithm to identify new members. We use the tangential velocities  $v_\alpha$  and  $v_\delta$  and their errors for determining the cuts of the training set. The tangential velocities were calculated through the parallaxes  $\varpi$  and proper motions  $\mu_\alpha^*$  and  $\mu_\delta$  using the following formulas:

$$v_\alpha = 4.74047 \cdot \mu_\alpha^* / \varpi \quad (\text{A.1})$$

$$v_{\alpha\_err} = 4.74047 \cdot \sqrt{\mu_{\alpha\_err}^{*2} / \varpi^2 + \mu_\alpha^{*2} \cdot \varpi_{err}^2 / \varpi^4} \quad (\text{A.2})$$

$$v_\delta = 4.74047 \cdot \mu_\delta / \varpi \quad (\text{A.3})$$

$$v_{\delta\_err} = 4.74047 \cdot \sqrt{\mu_{\delta\_err}^{*2} / \varpi^2 + \mu_\delta^{*2} \cdot \varpi_{err}^2 / \varpi^4} \quad (\text{A.4})$$

The cuts for the training set were determined by using plots as a visual aid. Figure A.1 shows plots of various properties of the complete literature sample in blue and sources that satisfy our chosen quality cuts in orange. We applied the following quality cuts for constructing the training set:

$$100 \text{ pc} < d < 180 \text{ pc} \quad (\text{A.5})$$

$$\varpi_{err} / \varpi < 0.2 \quad (\text{A.6})$$

$$-15 \text{ km/s} < v_r < 5 \text{ km/s} \quad (\text{A.7})$$

$$v_{r\_err} < 3 \text{ km/s} \quad (\text{A.8})$$

$$-10 \text{ km/s} < v_\alpha < 0 \text{ km/s} \quad (\text{A.9})$$

$$v_{\alpha\_err} < 3 \text{ km/s} \quad (\text{A.10})$$

$$-22 \text{ km/s} < v_\delta < -12 \text{ km/s} \quad (\text{A.11})$$

$$v_{\delta\_err} < 3 \text{ km/s} \quad (\text{A.12})$$

As the sources are located around a distance  $d$  of 140 pc, we apply a symmetrical distance range of 100 to 180 pc for the training set. A relative error-to-value cut is also applied for the parallax  $\varpi$ . Radial velocities  $v_r$  are mostly around a value of -5 km/s, so we apply a symmetrical range of -15 to 5 km/s. A relative error cut is not sensible for the radial velocities, since many of them are close to zero, which could lead to losing sources that actually belong to  $\rho$  Oph. Therefore, we apply an absolute radial velocity error cut. Since the errors of the tangential velocities  $v_\alpha$  and  $v_\delta$  are comparable to the radial velocity errors, similar cuts can be made in all three velocity directions. We apply the same absolute error cut to the tangential velocities, since several  $v_\alpha$  values are also close to zero. These conditions select sources that do not deviate much from the average values of the chosen properties, creating a suitable selection for finding new sources with similar properties.

## Appendix B: Gaia quality criteria

For the observational HRD in Figure 7, we apply quality cuts to *Gaia* sources in order to reduce contamination by inferior data, similar to the cuts used in Großschedl et al. (2020). Further details on the *Gaia* parameters can be found on the official website of the mission: <https://gea.esac.esa.int/archive/documentation/index.html>. We applied the following quality criteria to *Gaia* sources:

$$\varpi_{err} / \varpi < 0.2 \quad (\text{B.1})$$

$$\text{ruwe} < 1.4 \quad (\text{B.2})$$

$$G_{err} < 0.05 \text{ mag} \quad (\text{B.3})$$

$$\text{visibility\_periods\_used} > 6 \quad (\text{B.4})$$

$$\text{astrometric\_sigma5d\_max} < 1.4 \quad (\text{B.5})$$

The  $G_{err}$  value is defined as:

$$G_{err} = 1.0857 \cdot \text{phot\_g\_mean\_flux\_error} / \text{phot\_g\_mean\_flux} \quad (\text{B.6})$$

## Appendix C: Contamination fraction constraint

Following Ratzenböck et al. (2020), we seek to constrain the contamination fraction of predicted sources across models. As discussed in Sect. 3, the contamination fraction is determined via the 3D velocity distribution of  $\rho$  Oph candidate sources. However, for single models we observe few sources that feature radial velocity measurements in the prediction set, which leads to a marginal effect of the contamination fraction prior assumption on the number of rejected models. This effect is highlighted in Figure C.1, where we see that over 99 % of models adhere to the contamination rule across various maximal threshold values. For each contamination threshold value we sample 20 models where we have set the maximal number of samples to 800 and sampled the remaining prior assumptions within their respective ranges (see Sect. 3 for more details). The reported accepted model fraction constitutes a mean value across the 20 sampled prior assumption tuples. The standard deviation is negligibly small.

## Appendix D: Sampling in prior assumption space

Following the discussion in Sect. 3, we randomly sample 100 prior assumption tuples within their respective range, which results in 100 model ensembles. In Figure D.1 the distribution in the number of inferred sources and contamination fraction space of these ensemble classifiers is shown. The prior assumption space of the maximal positional extent (left column), the maximal velocity extent (middle column) and the maximal systematic shift (right column) was uniformly sampled within their respective ranges. We use color to encode the maximal prior assumption value in this space. On the bottom the sampled prior assumption distributions for models showing minimal contamination (in purple) and remaining models (in gray) can be seen. For models with low contamination we observe a tendency to lower maximal extents in position and velocity space, but a systematic shift with a mode at around 0.28.

## Appendix E: Stability

We discuss the stability of the predicted sources as well as the stability cut we chose. Although the model selection process via a set of prior assumptions (see Sect. 3) removes a majority of unsuitable models, the lack of a clear objective function still leaves some contamination in our final prediction sample. In order to find a set of high fidelity members, we study the prediction frequency, or stability, of the inferred sources across the model ensemble. Figure E.1 shows a histogram of the stability of the known and new sources. Both of them show a relatively similar stability distribution. Many of the known sources from the literature are predicted with a stability of 0 because they are not in the *Gaia* EDR3 catalog.

As discussed in Ratzenböck et al. (2020), an appropriate stability threshold should reduce spurious sources while maximizing the number of legitimate cluster members. For this purpose, the authors studied the impact of the stability criterion on the Cartesian velocity dispersion and selected an optimal value by eye. Now we aim to train multiple model ensembles under different prior assumptions and jointly attempt to characterize

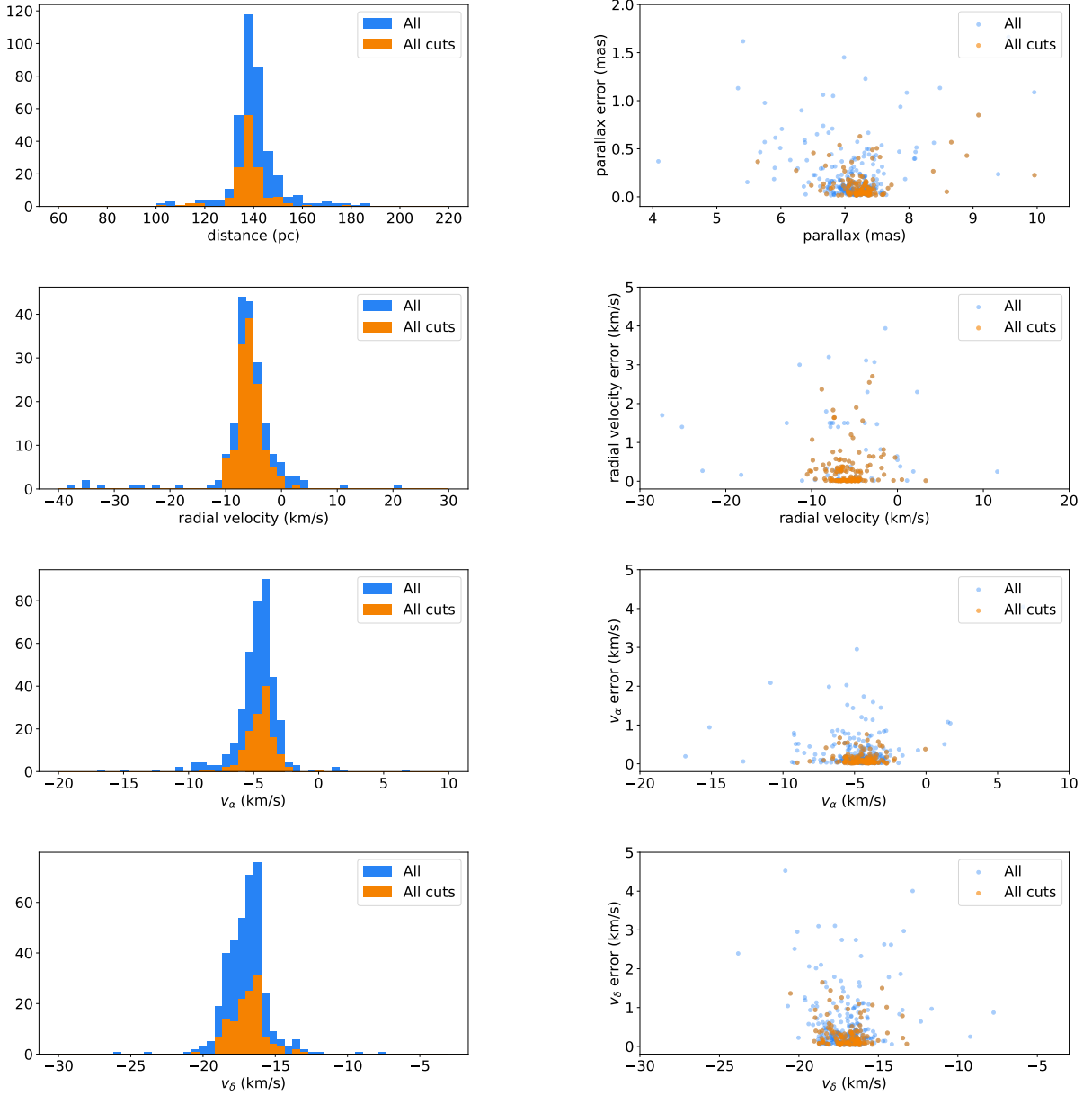


**Fig. A.1:** Plots of various properties of the  $\rho$  Oph literature sample shown in blue, while the sources that fulfill all of the quality cuts are shown in orange. These plots were used as a visual aid to determine the cuts for the training set.

each model ensemble corresponding to a single prior belief tuple in terms of a contamination estimate and the number of identified points at their respective optimal stability thresholds (see Sect. 3). Therefore, we intend to automatically determine a threshold value for each model ensemble. To do so we consider the following. The distribution of inferred members and training members in 5D is by design very close and adheres to our prior assumptions, so we cannot infer an independent quality criterion from the prediction in 5D. But since stars that are born together move together (Kamdar et al. 2019), we can similarly to Ratzenböck et al. (2020) use the, albeit sparsely available, full 3D velocity information for determining the stability criterion.

To be co-moving, we postulate that inferred sources with radial velocity information should be distributed as similarly as possible to the training set 3D velocities. To test this similarity,

we model the 3D velocity data using a multivariate normal distribution. We determine the mean and covariance by maximizing the likelihood of the training data under the model. To estimate the difference between the trained and inferred sources we use the Kullback–Leibler (KL) divergence (Kullback & Leibler 1951)  $D_{\text{KL}}(p \parallel q)$  where  $q$  and  $p$  both constitute probability distribution functions. The KL divergence of  $p(x)$  from  $q(x)$  of the continuous variable  $x$  is defined via

$$D_{\text{KL}}(p \parallel q) = \int_{-\infty}^{\infty} p(x) \log \left( \frac{p(x)}{q(x)} \right). \quad (\text{E.1})$$

It can be interpreted as the information content that is lost when the true distribution  $p$  is substituted by an approximate distribution  $q$  (Burnham & Anderson 2002). Here,  $p$  represents our training set distribution, while the approximate distribution  $q$  describes the distribution of inferred sources. To evaluate

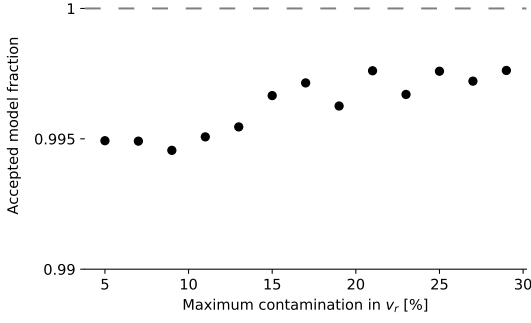


**Fig. C.1:** Accepted model fraction according to various maximal contamination requirements. The prior assumption value is varied between 5 % and 30 %. We find no significant impact of the contamination fraction restriction for individual models on the number of accepted models.

$D_{\text{KL}}(p \parallel q)$ , we model  $q$ , the velocity distribution of the derived members, assuming a single Gaussian. For two multivariate normal distributions, the KL divergence can be written analytically in the following form (Petersen & Pedersen 2012):

$$D_{\text{KL}} = \frac{1}{2} \left[ \log \frac{|\Sigma_q|}{|\Sigma_p|} - d + \text{tr}(\Sigma_q^{-1} \Sigma_p) + (\mu_q - \mu_p)^T \Sigma_q^{-1} (\mu_q - \mu_p) \right] \quad (\text{E.2})$$

Here,  $\mu$  and  $\Sigma$  refer to the mean and covariance matrices of the multivariate normal distributions, respectively. The variable  $d$  describes the number of dimensions, which is in this case  $d = 3$ . In order to find the optimal stability threshold we seek to minimize the KL divergence between the Cartesian velocity distribution of training and inferred sample populations, which is illustrated in Figure E.2. We find an optimal threshold criterion of stability  $> 13$  %. The stability is included in our final catalog shown in Table I.1.

## Appendix F: Validation of inferred sources in the HRD

As a final validation step, we compare the inferred source distribution to the training set distribution in the HRD. Since both populations should be co-eval, we can characterize the HRD distribution by their deviation from the best fitting isochrone on the training set. In Figure F.1, the standard deviation of residuals between the data and the 5 Myr isochronal curve is shown. We find no significant difference between the training set members and the inferred sources based on their HRD distributions.

## Appendix G: Astrometric properties of known and new sources

Table G.1 shows the average astrometric properties of the sources in  $\rho$  Oph, such as the distances, proper motions, radial and tangential velocities, Galactic Cartesian positions  $X, Y, Z$  and Galactic Cartesian velocities  $U, V, W$ , as well the standard deviations ( $1\sigma$ ) of these parameters. These average values were determined for the known and new sources, as well as for all of them together. To avoid the influence of outliers, impostors defined in Sect. 2.2 are not included in the calculations. The column  $\Delta$

**Table G.1:** Average positional and dynamical properties including their standard deviations ( $1\sigma$ ) for the sources in  $\rho$  Oph. The average values were determined for the known and new sources separately, as well as for all of them together. The column  $\Delta$  contains the difference of the known and new mean values for comparison of the two.

Dimension	Known	New	All	$\Delta$
$\alpha$ (deg)	246.9 $\pm$ 1.0	246.1 $\pm$ 1.3	246.7 $\pm$ 1.1	0.8
$\delta$ (deg)	-24.3 $\pm$ 0.6	-24.5 $\pm$ 1.1	-24.3 $\pm$ 0.8	0.2
$\varpi$ (mas)	7.2 $\pm$ 0.5	7.1 $\pm$ 0.4	7.2 $\pm$ 0.4	0.1
$d$ (pc)	139.8 $\pm$ 8.6	141.4 $\pm$ 4.2	140.5 $\pm$ 7.2	-1.6
$\mu_\alpha^*$ (mas/yr)	-7.2 $\pm$ 2.5	-8.4 $\pm$ 2.0	-7.7 $\pm$ 2.4	1.2
$\mu_\delta$ (mas/yr)	-25.2 $\pm$ 3.0	-24.7 $\pm$ 1.9	-25.0 $\pm$ 2.7	-0.5
$v_\alpha$ (km/s)	-4.6 $\pm$ 1.2	-5.7 $\pm$ 1.4	-5.1 $\pm$ 1.4	1.1
$v_\delta$ (km/s)	-17.0 $\pm$ 1.2	-16.5 $\pm$ 1.1	-16.8 $\pm$ 1.2	-0.5
$v_r$ (km/s)	-5.2 $\pm$ 3.4	-7.2 $\pm$ 3.0	-5.5 $\pm$ 3.4	2.0
$X$ (pc)	132.8 $\pm$ 8.2	133.9 $\pm$ 4.3	133.2 $\pm$ 6.9	-1.1
$Y$ (pc)	-15.6 $\pm$ 1.6	-17.1 $\pm$ 2.3	-16.3 $\pm$ 2.0	-1.5
$Z$ (pc)	40.8 $\pm$ 2.9	41.8 $\pm$ 3.2	41.2 $\pm$ 3.1	-1.0
$U$ (km/s)	-4.7 $\pm$ 3.0	-6.7 $\pm$ 2.9	-5.0 $\pm$ 3.1	2.0
$V$ (km/s)	-15.2 $\pm$ 1.2	-15.2 $\pm$ 0.8	-15.2 $\pm$ 1.1	0.0
$W$ (km/s)	-9.0 $\pm$ 1.5	-8.7 $\pm$ 1.5	-9.0 $\pm$ 1.5	-0.3

contains the difference of the known and new mean values for comparison.

There appear to be only small deviations between the properties of the known and new sources, which are not significant within  $1\sigma$ . This further confirms that, on average, they belong to the same region. The average values of  $\rho$  Oph for  $\varpi, \mu_\alpha^*, \mu_\delta, X, Y, Z$  agree relatively well with those determined by Cánovas et al. (2019) within  $1\sigma$ .

## Appendix H: Observational HRD of the two populations in $\rho$ Oph

Figure H.1 shows an observational HRD of the two dynamical populations in  $\rho$  Oph *Gaia* EDR3 photometry. The first population (Pop 1), which comprises the clusters of young stars around the  $\rho$  Ophiuchi star and the main Ophiuchus clouds (L1688, L1689, L1709), is shown in red. The second dynamically distinct population (Pop 2), is shown in yellow. As in Figure 7, corrections were applied to the *Gaia*  $G$  passband as described in Riello et al. (2020). To include only high quality measurements, the quality cuts described in Appendix B were applied to the photometry. We show isochrones for 1, 3 and 10 Myr (Marigo et al. 2017), as well as an extinction vector  $A_V$  in the  $V$  passband, determined with the reddening law for the  $G, BP$  and  $RP$  passbands from Cardelli et al. (1989) and O'Donnell (1994) provided by PARSEC. Two equal-mass-curves for sources with 0.09  $M_\odot$  (solar masses) and 1  $M_\odot$  are shown in orange.

We use  $G_{BP} - G_{RP}$  instead of  $G - G_{RP}$  in this HRD because it shows a clearer separation between the two populations. It is easier to see in  $G_{BP} - G_{RP}$  that the second population is in general older than the first and aligns better with the older isochrone of 10 Myr. The blueshifted tail in Figure H.1 is due to erroneous photometry and does not show when using  $G - G_{RP}$ , which is the reason why we used  $G - G_{RP}$  for Figure 7.

## Appendix I: $\rho$ Oph catalog overview

In this Appendix, we present our final catalog of  $\rho$  Oph sources, which is available online at the CDS. It includes all known



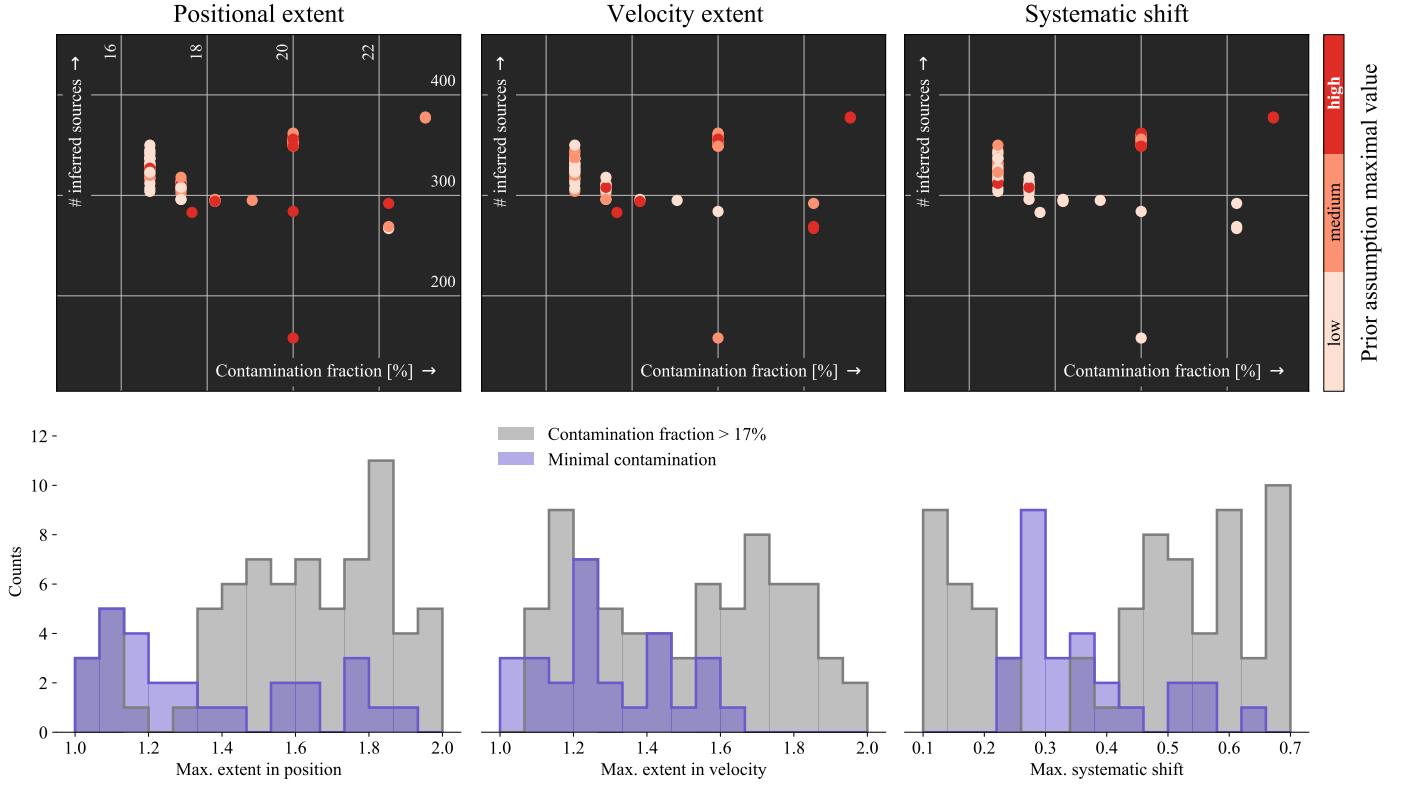


**Fig. D.1:** *Top.* Distribution of 100 ensemble classifiers trained using various prior assumption constraints in the number of inferred sources and contamination fraction space. We have randomly sampled the prior assumption of the maximal positional extent (left column), the maximal velocity extent (middle column) and the maximal systematic shift (right column) within their respective ranges. The color highlights the maximal prior assumption value.

*Bottom.* Sampled prior assumption distributions for models showing minimal contamination (in purple) and remaining models (in gray). For models with low contamination we observe a tendency to lower maximal extents in position and velocity space, but a systematic shift with a mode at around 0.28.

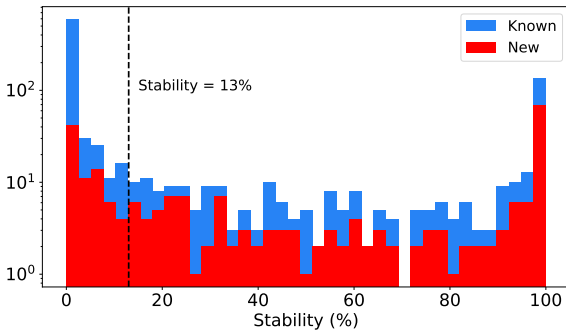


**Fig. E.1:** The stability (in percent), of the known and new sources, as determined by the OCSVM method.

sources from the literature and all sources identified by the OCSVM, even those with a stability < 13, resulting in a total of 1011 sources. Table 1.1 shows an overview of the column names, their units and their descriptions. In total, our catalog contains 59 columns. The column “Ref” serves as a reference for the literature sources, where each paper is cited by their reference number given in Table 1. Several sources were obtained from more than one paper, therefore some sources have more than one reference number.

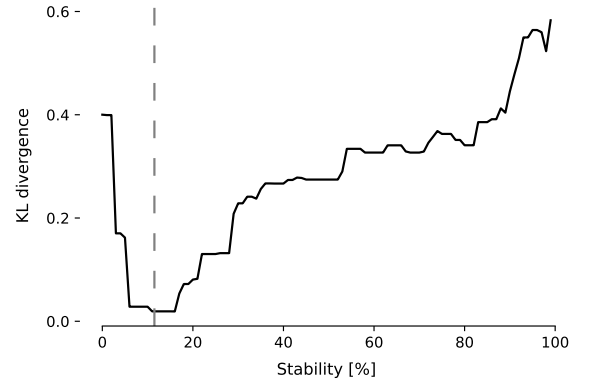


**Fig. E.2:** KL divergence between Cartesian velocity distributions of training and inferred source populations determined across various stability threshold values. We find an optimal threshold criterion of stability > 13 % for the final ensemble across various prior assumptions which produce minimal contamination (see Sect. 3 for a more detailed discussion).

Since the known sources have astrometric properties obtained from the literature, *Gaia* EDR3, APOGEE-2, or *Gaia*-ESO, we provide the column “Ref\_pm\_plx\_rv” for the reference of the proper motions, parallax and radial velocity values, respectively. Each row contains three numbers for citation

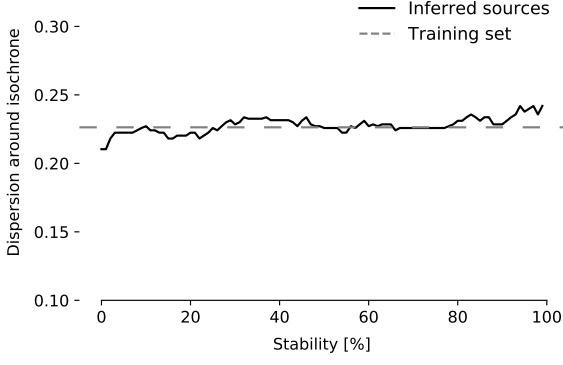


**Fig. F.1:** Comparison between the training and inferred sources across the full stability range. The y-axis shows the standard deviation of residuals between the data and an isochrone of 5 Myr, describing the best fit to the training data. We find no significant difference between the training set members and the inferred sources based on their HRD distributions.

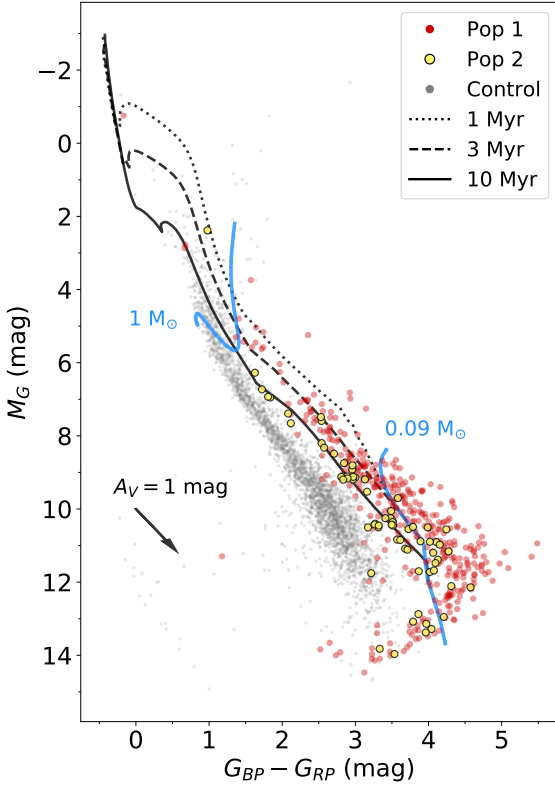


**Fig. H.1:** Observational HRD of the two populations in  $\rho$  Oph, and the control sample in gray, with corrections applied to the  $G$  passband. An extinction vector with  $A_V = 1$  mag is shown as a black arrow. The isochrones correspond to ages of 1, 3 and 10 Myr, while the iso-mass lines of  $0.09 M_\odot$  and  $1 M_\odot$  include stars with ages from 0.1 to 100 Myr.

of these values, where “1”, “2”, “3”, and “4” signify measurements obtained from the literature, *Gaia* EDR3, APOGEE, and *Gaia*-ESO, respectively. “0” implies that a source does not have a corresponding proper motion, parallax or radial velocity measurement.

**Table I.1:** Column overview of the final catalog containing known and new  $\rho$  Oph sources.

Column Name	Unit	Description
source_id_edr3	-	<i>Gaia</i> EDR3 ID
ra	deg	Right ascension (J2000)
dec	deg	Declination (J2000)
l	deg	Galactic longitude
b	deg	Galactic latitude
parallax	mas	Parallax
parallax_error	mas	Parallax error
distance	pc	Distance, determined from the inverse of the parallax
pmra	mas/yr	Proper motion in ra direction
pmra_error	mas/yr	Error in pmra
pmdec	mas/yr	Proper motion in dec direction
pmdec_error	mas/yr	Error in pmdec
radial_velocity	km/s	Heliocentric radial velocity
radial_velocity_error	km/s	Error in radial velocity
v_alpha	km/s	Tangential velocity in ra direction
v_alpha_error	km/s	Error in v_alpha
v_delta	km/s	Tangential velocity in dec direction
v_delta_error	km/s	Error in v_delta
X	pc	Galactic Cartesian X position component
Y	pc	Galactic Cartesian Y position component
Z	pc	Galactic Cartesian Z position component
U	km/s	Galactic Cartesian U velocity component
V	km/s	Galactic Cartesian V velocity component
W	km/s	Galactic Cartesian W velocity component
ppm	mas/yr	proper motion vector, $\sqrt{\text{pmra}^2 + \text{pmdec}^2}$
angle	deg	angle of ppm to ra-axis
ruwe	-	Renormalized unit weight error
astrometric_sigma5d_max	mas	Longest principal axis in the 5-dimensional error ellipsoid
astrometric_params_solved	-	Which parameters have been solved for
visibility_periods_used	-	Number of visibility periods in the astrometric solution
phot_g_mean_flux	e-/s	Error on G-band mean flux
phot_g_mean_flux_error	e-/s	G-band mean flux
phot_g_mean_mag	mag	G-band mean magnitude
phot_bp_mean_mag	mag	Integrated BP mean magnitude
phot_rp_mean_mag	mag	Integrated RP mean magnitude
Train	-	=1 for sources in the training set
Predict	-	=1 for predicted sources in <i>Gaia</i> EDR3
New	-	=1 for new sources in <i>Gaia</i> EDR3
Stability	-	Stability of the sources, range: 0–100
Impostors	-	=1 for impostor sources
Suspicious	-	=1 for suspicious sources
Pop1	-	=1 for sources of the first population
Pop2	-	=1 for sources of the second dynamically distinct population
designation_2MASS	-	2MASS ID
j_h	mag	J–H color
h_k	mag	H–K color
j_k	mag	J–K color
designation_WISE	-	WISE ID
w1mpro	mag	WISE W1 magnitude
w1snr	-	W1 signal-to-noise ratio
w2mpro	mag	WISE W2 magnitude
w2snr	-	W2 signal-to-noise ratio
w3mpro	mag	WISE W3 magnitude
w3snr	-	W3 signal-to-noise ratio
APOGEE_ID	-	APOGEE ID
Ref	-	Reference for literature sources, see Table 1, range: 1–11
Ref_pm_plx_rv	-	Reference for proper motions, parallax and radial velocity

**Notes.** Column overview of the final catalog of  $\rho$  Oph sources, which includes the known sources from the literature as well as the new sources identified by the algorithm. The complete table is available for download at the CDS.

